



Cite this: *RSC Appl. Interfaces*, 2025, 2, 1715

## Nanoengineered $\text{Mn}_3\text{O}_4/\text{rGO}$ electrophotocatalyst with dual functionality for detection of 2,4,6-trichlorophenol and degradation of methylene blue dye in environmental monitoring and cleanup

Diksha Singh,<sup>a</sup> Anshu Kumar Singh,<sup>a</sup> Ranjana Verma<sup>b</sup> and Jay Singh  <sup>\*a</sup>

Here, we report the hydrothermal synthesis of  $\text{Mn}_3\text{O}_4$  nanomaterial and  $\text{Mn}_3\text{O}_4/\text{rGO}$  nanocomposite (rGO, reduced graphene oxide). The prepared nanocomposite (NC) was electrophoretically deposited (EPD) on indium tin oxide (ITO) to fabricate the  $\text{Mn}_3\text{O}_4/\text{rGO}/\text{ITO}$  electrode, which is further utilized for the electrochemical estimation of 2,4,6-trichlorophenol (2,4,6-TCP). The charge transfer rate constant, diffusion coefficient ( $D$ ), and surface concentration values evaluated for the  $\text{Mn}_3\text{O}_4/\text{rGO}/\text{ITO}$  electrode are  $0.53\text{ s}^{-1}$ ,  $0.86 \times 10^{-6}\text{ mol cm}^{-2}$ , and  $0.358\text{ cm}^2\text{ s}^{-1}$ , respectively. The electrochemical sensor displays a linear extent of 2,4,6-TCP detection from 1 to  $500\text{ }\mu\text{M}$  with a limit of detection (LoD) of  $0.038\text{ }\mu\text{M}$  and sensitivity of  $2.17\text{ }\Omega\text{ }\mu\text{M}^{-1}\text{ cm}^{-2}$ . Here, we demonstrate the 2,4,6-TCP detection via electrochemical impedance spectroscopy (EIS) sensing and photocatalytic degradation, as well as the kinetics of methylene blue (MB) dye, analyzed in parallel with bare  $\text{Mn}_3\text{O}_4$  under UV light irradiation. The results indicate that  $\text{Mn}_3\text{O}_4/\text{rGO}$  NCs have preferred MB photodegradation efficacy with a reaction rate constant and low degradation time compared to bare  $\text{Mn}_3\text{O}_4$  nanomaterials (NMs). The rate constants for the  $\text{Mn}_3\text{O}_4$  and  $\text{Mn}_3\text{O}_4/\text{rGO}$  NCs were found to be  $0.00075$  and  $0.0197$ , respectively, and the MB dye degradation reached up to 6% with the  $\text{Mn}_3\text{O}_4$  catalyst and up to 80% with the  $\text{Mn}_3\text{O}_4/\text{rGO}$  catalyst when exposed to UV light for 80 minutes.

Received 22nd May 2025,  
Accepted 31st July 2025

DOI: 10.1039/d5lf00149h  
[rsc.li/RSCApplInter](http://rsc.li/RSCApplInter)

## 1. Introduction

Water is vital for every single life form. Recently, water quality has deteriorated due to rapid industrialization, with dyes and phenolic compounds posing major pollution threats attributable to their high solubility and stability in water.<sup>1,2</sup> Multiple phenolic compounds are employed as fungicides and herbicides and exist in industrial wastewater. Owing to their bioaccumulation, poor biodegradability, high stability, and toxicity, they pose intense environmental and biological health concerns. There is a need for the cleanup of such contaminants for environmental remediation; here, we employ layered and self-assembled  $\text{Mn}_3\text{O}_4/\text{rGO}$  NCs for this purpose. Methylene blue (MB) is a standard cationic aromatic azo dye and a water pollutant. MB is prevalent in water pollutants from industries like textile, plastic, leather, and food, posing environmental risks due to their widespread use.<sup>3</sup> 2,4,6-Trichlorophenol (2,4,6-TCP), an organochlorine

pesticide, has been utilized as an antifungal and antimicrobial agent, an antiseptic,<sup>3–5</sup> a preservative for leather and glue in the cellulose and paper industry, and as a mold inhibitor<sup>4</sup> since the 1920s. In the present scenario, 2,4,6-TCP is also utilized in wineries to disinfect barrels and protect cork and wood.<sup>5,6</sup> As 2,4,6-TCP has an aryl structure and chlorine atoms, it disturbs aquatic creatures and is also a cause of cancer and mutation in humans.<sup>7,8</sup> Despite that, 2,4,6-TCP is a weak acid as well as a renowned carcinogenic, toxic, and mutagenic pollutant. 2,4,6-TCP feasibly enters the epidermis of humans and is effortlessly transported across the intestinal tract.<sup>9,10</sup> The discharge of dyes and 2,4,6-TCP into water causes contamination, harming aquatic life by blocking light. Exposure to MB can lead to nausea, sweating, vomiting, mental disorders, allergies, and respiratory issues.<sup>11</sup> Identification and extraction of analogous organic pollutants are exclusively crucial to regulating water pollution. Over the years, conventional approaches have been applied for the eradication of organic pollutants, like adsorption on activated charcoal, coagulation, reverse osmosis, deposition, biological management, etc., yet these approaches have some limitations. Moreover, adsorption procedures require further accessory treatment procedures for the regeneration of the adsorbent materials.<sup>12</sup> All these trials brought about the

<sup>a</sup> Department of Chemistry, Institute of Sciences, Banaras Hindu University, Varanasi 221005, Uttar Pradesh, India. E-mail: [jaysingh.chem@bhu.ac.in](mailto:jaysingh.chem@bhu.ac.in), [jainmnit@gmail.com](mailto:jainmnit@gmail.com); Tel: Phone: +91 9871766453

<sup>b</sup> Department of Mechanical Engineering, Indian Institute of Technology, Banaras Hindu University (IIT-BHU), Varanasi 221005, Uttar Pradesh, India



acceptance of the advanced oxidation process (AOP) for the degradation of contaminants from sources of water.<sup>13</sup> Among varied AOP strategies, photocatalytic degeneration of organic pollutants consuming semi-conductive metal oxides, namely  $\text{Mn}_3\text{O}_4/\text{rGO}$ ,  $\text{TiO}_2$ ,  $\text{Fe}_2\text{O}_3$ ,  $\text{ZnO}$ , and  $\text{CdO}$ ,<sup>14</sup> has acquired vast eminence due to the probability of entire organic contaminants being mineralized in a hydrous environment.<sup>15</sup> The EPA categorizes 2,4,6-TCP as a highly hazardous carcinogen (group B2). It can adulterate beverages owing to remnants in the filling stuff.<sup>7</sup> Sensory tests ascertain levels above 2.0 ppb, while chromatographic approaches are conventionally liable for investigation.<sup>16,17</sup> Chlorophenols are extensive contaminants found in soil, water, and wastewater, as well as in living specimens. 2,4,6-TCP is a predominant pollutant prohibited by the USEPA.<sup>18</sup> Due to its stability, persistence, toxicity, and carcinogenic potential, 2,4,6-TCP poses a prolonged threat to biology and the environment, leading to its regulation by the European Union. Developing a quick, precise, and effective recognition method is indispensable for research applications.<sup>19</sup> Xiaolin Zhu and Kexin Zhang, *et al.*, and the US Environmental Protection Agency (USEPA) locate it in the priority pollutants lists.<sup>8</sup> The ultimately determined acceptable concentration of CPs in potable water by the US Environmental Protection Agency and the European Union is 1 and 0.5 ppb, respectively. 2,4,6-TCP belongs to prominent threatening and toxic chlorinated organic compounds (CPs) for the environment. CPs exhibit unwanted consequences at low concentrations of  $0.1 \text{ mg L}^{-1}$  in drinking water.<sup>20,21</sup> Varied sophisticated traditional methods, comprising capillary electrophoresis, fluorescence, high-performance liquid chromatography (HPLC),<sup>22</sup> gas chromatography, mass spectrometry,<sup>23</sup> and spectrometry,<sup>24</sup> have been utilized for 2,4,6-TCP detection. These techniques are tedious and require extensive instrumentation and technical expertise. Electroanalytical procedures recommend an efficient as well as faster substitute for detection, permitting direct, pretreatment-free measurements in complex matrices.<sup>25,26</sup> A method is considered suitable only after validation, which involves the assessment of linearity, precision, selectivity, LoD, LOQ, and accuracy. The electrochemical technique demonstrates the excellent supremacy of fast detection response and ease of sample preparation, which assists a broad range of catalyst materials,<sup>27</sup> acceptable reproducibility, and low instrument cost.<sup>28</sup> The structure of the surface and active sites available on nanomaterials (NMs) turns on the activity of the NMs,<sup>29</sup> which are conceivably utilized as active sites for the enhancement of the electrocatalytic performance of the electrode.<sup>30</sup> Due to their unique physical, optical, and electrochemical attributes, manganese oxide NMs are favorably considered for biomolecule detection. They promote a large area for interaction, a high rate for charge transfer, non-toxicity, and low cost. Structural versatility, as well as the existence of multiple oxidation states (+2, +3) of  $\text{Mn}_3\text{O}_4$  within the uniform crystalline structure, make it appropriate for diverse applications like photocatalytic activity and

electrocatalytic degradation of pollutants, as  $\text{Mn}_3\text{O}_4$  produces reactive species that oxidize and disintegrate the contaminants, assisting in wastewater treatment and environmental remediation. Nguyen *et al.* reported that the biosensor's electrochemical performance improves after integrating rGO into transition metal oxide, making the electrode material more conductive.<sup>31</sup> As  $\text{Mn}_3\text{O}_4/\text{rGO}$  generates reactive oxygen species in the presence of light, it can exhibit antibacterial and antiviral properties, making it suitable for surface disinfection and water treatment. During the combination of  $\text{Mn}_3\text{O}_4$  and rGO, the synergistic interaction of  $\text{Mn}_3\text{O}_4$  and rGO improves electrocatalytic<sup>32</sup> and photocatalytic performance. The efficient transfer of photogenerated electrons from  $\text{Mn}_3\text{O}_4$  to rGO is feasible due to the excellent electron acceptor and transporter properties, which lower recombination and enhance photocatalytic efficiency. As rGO acts as a support matrix, it prevents the aggregation of  $\text{Mn}_3\text{O}_4$  NMs and ensures their high dispersion as well as availability<sup>33</sup> and high surface area. As we incorporate rGO, it improves the stability and reusability of photocatalysts because it makes NCs less susceptible to photo corrosion and sustains their catalytic activity across multiple cycles of operation. Adaptability of having numerous oxidation states (+2, +3) of  $\text{Mn}_3\text{O}_4$  in the homogeneous crystalline structure. Here,  $\text{Mn}^{2+}$  and  $\text{Mn}^{3+}$  cations exist in tetrahedral and octahedral sites, respectively. From the XRD study, it was noticed that the particle size decreases as we incorporate rGO into the  $\text{Mn}_3\text{O}_4$  NMs and synthesize  $\text{Mn}_3\text{O}_4/\text{rGO}$  NCs, which facilitates improvement and enhancement in surface area. From the UV-visible study, we observed that the band gap increases in NCs ( $\text{Mn}_3\text{O}_4/\text{rGO}$  BE = 4.03 eV) as compared to  $\text{Mn}_3\text{O}_4$  NMs (BE = 3.86 eV), which is validated from the XRD study as well, *i.e.*, size decreases, then band gap increases (quantum confinement effect; according to this, as the size of the material decreases, the band gap increases).

Here, we employed a hydrothermal procedure for the synthesis of  $\text{Mn}_3\text{O}_4$  and  $\text{Mn}_3\text{O}_4/\text{rGO}$  NCs, and  $\text{Mn}_3\text{O}_4/\text{rGO}$  NCs are further applied for the detection of 2,4,6-TCP, employing an electrochemical strategy and photocatalytic degradation of MB dye. Here, distinct electrochemical methodologies like cyclic voltammetry (CV) and differential-pulse voltammetry (DPV) were liable to support varied electrochemical analyses during the electrochemical study. However, EIS was utilized for the electrochemical determination of 2,4,6-TCP on the  $\text{Mn}_3\text{O}_4/\text{rGO}/\text{ITO}$  electrode in the concentration range from 1 to 500  $\mu\text{M}$ .

## 2. Experimental details

### 2.1. Chemicals and reagents

The chemicals that were employed for the synthesis of  $\text{Mn}_3\text{O}_4$  NMs and  $\text{Mn}_3\text{O}_4/\text{rGO}$  NCs are manganese acetate tetrahydrate [Merck], polyethylene glycol (PEG) [CDH], NaOH



[Merck], 25% NH<sub>3</sub> solution [Merck], graphite flakes, H<sub>2</sub>SO<sub>4</sub> (98%) [Merck], HNO<sub>3</sub> (69%) [Merck], glass sheets of indium tin oxide (ITO) (surface resistivity 20 Ω Sq<sup>-1</sup>). Furthermore, K<sub>4</sub>[Fe(CN)<sub>6</sub>]<sup>3</sup>·3H<sub>2</sub>O, K<sub>3</sub>[Fe(CN)<sub>6</sub>]<sup>4</sup>, [Na<sub>2</sub>HPO<sub>4</sub>·2H<sub>2</sub>O] (99%), [NaH<sub>2</sub>PO<sub>4</sub>·2H<sub>2</sub>O] (98–100.5%), NaCl (99%), and methylene blue stain were obtained from Merck Specialties Private Ltd., Mumbai, India. AR grade 2,4,6-TCP used for the electrochemical specification was acquired from Sigma-Aldrich. The different pH buffer solutions were formed solely utilizing Milli-Q water for the duration of the experiments.

## 2.2. Synthesis of Mn<sub>3</sub>O<sub>4</sub>/rGO NCs

Hummer's approach was modified to prepare GO. 0.30 mg of prepared GO was thoroughly dissolved in distilled water in a beaker. 5 mL of polyethylene glycol (PEG), a surfactant, was magnetically stirred overnight after the addition of a 25% NH<sub>3</sub> solution dropwise, until the pH reached approximately 12, to reduce GO into rGO, and this procedure was also further utilized with Mn metal precursor and synthesized GO for the *in situ* preparation of Mn<sub>3</sub>O<sub>4</sub>/rGO NCs. For the preparation of Mn<sub>3</sub>O<sub>4</sub>/rGO NCs, 0.30 mg of prepared GO was thoroughly dissolved in distilled water in a beaker. Following 2 hours of vigorous magnetic stirring, 60 mL of a 0.2 M manganese acetate solution was added to 15 mL of a 0.30 mg dispersion. 5 mL of PEG was then introduced to the reaction mixture. After that, a brown precipitate formed, and the mixture was magnetically stirred overnight after the addition of a 25% NH<sub>3</sub> solution dropwise, until the pH reached approximately 12. The next step involved placing the brown mixture into a Teflon-lined autoclave and heating it in an oven for 15 hours at 180 °C. Subsequently, a distilled water and

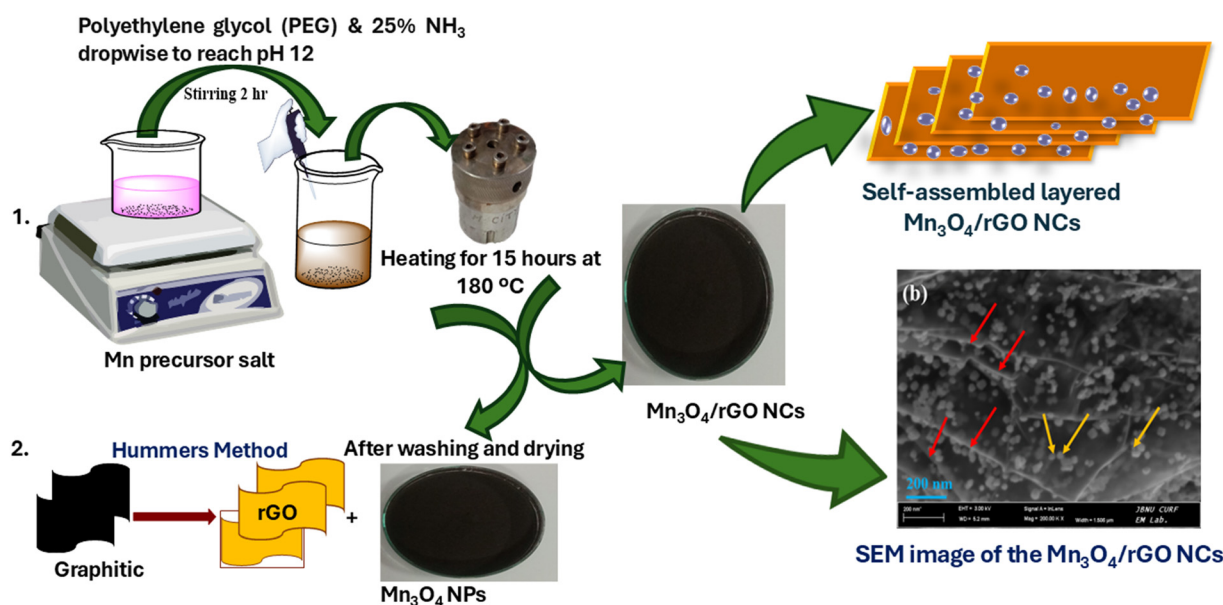
ethanol mixture was utilized during washing to remove impurities and dry the precipitate. In contrast, the same process was used to prepare bare Mn<sub>3</sub>O<sub>4</sub> without adding rGO, which is displayed in Scheme 1, along with the synthesized self-assembled layered Mn<sub>3</sub>O<sub>4</sub>/rGO NCs' SEM image.

## 2.3. Preparation of standard stock solution of 2,4,6-TCP

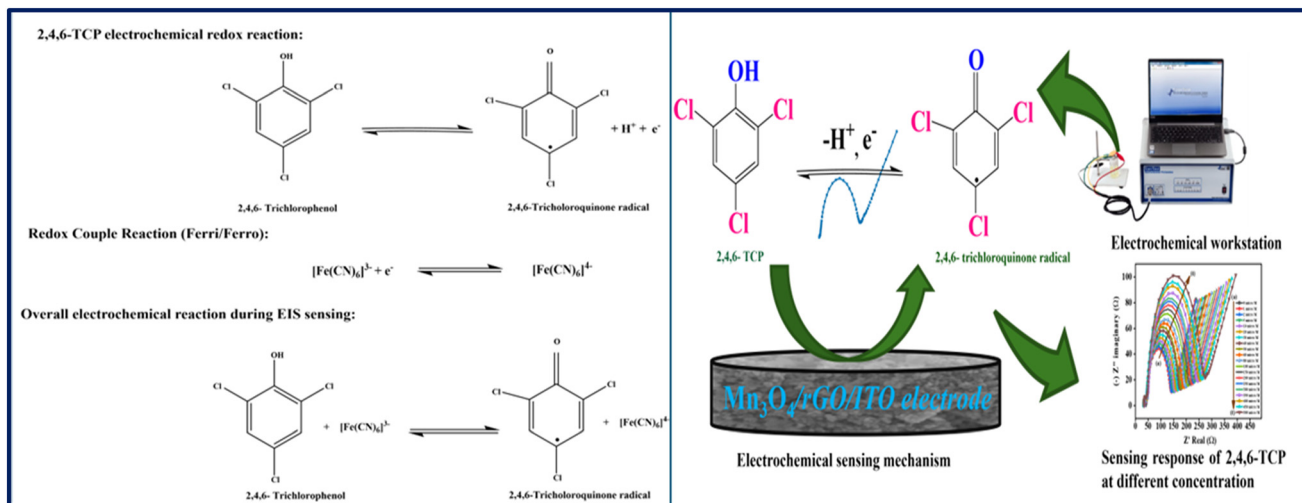
First, we prepared a 2,4,6-TCP stock solution in ethanol at a concentration of 10 mM. Afterward, the prepared stock solution was diluted with ethanol to prepare analytes at various concentrations.

## 2.4. Sensing phenomenon of 2,4,6-TCP on ITO

The electrochemical interface and oxidation mechanism of 2,4,6-TCP on Mn<sub>3</sub>O<sub>4</sub>/rGO/ITO electrode is shown in Scheme 2. During sensing, 2,4,6-TCP is oxidized to 2,4,6-trichloroquinone. The electrochemical methodology of 2,4,6-TCP is associated with significant steps that raise sensitivity and selectivity. The electrode modification is accompanied by Mn<sub>3</sub>O<sub>4</sub> NMs and Mn<sub>3</sub>O<sub>4</sub>/rGO NCs to improve 2,4,6-TCP detection. 2,4,6-TCP molecules adsorb on the modified electrode *via* interactions such as hydrogen bonding, π-π stacking, or electrostatic forces. Adsorbed 2,4,6-TCP employing electrochemical oxidation or reduction *via* electron transfer depends on the electrolyte pH. The electron transfer initiates a resistance proportional to the 2,4,6-TCP concentration, determined by the sensor. Here, we utilized techniques like EIS to provide a characteristic Nyquist plot. The resistance reciprocity is examined using calibration curves to ascertain the 2,4,6-TCP concentration. The electrode modification ensures selectivity and amplifies



**Scheme 1** Diagrammatic representation of (1) Mn<sub>3</sub>O<sub>4</sub> and (2) Mn<sub>3</sub>O<sub>4</sub>/rGO NC preparation *via* the hydrothermal method and SEM micrograph of the equivalent NCs.



**Scheme 2** Pictorial illustration of the electrochemical detection procedure of 2,4,6-TCP at distinct concentrations.

sensitivity *via* enlarging the surface area as well as improving electron transfer kinetics. Scheme 2 illustrates the electrochemical sensing mechanism of 2,4,6-TCP electrochemical redox couples. The electrochemical redox reaction on the modified electrode is as follows.

### 3. Results and discussion

#### 3.1. XRD study

An XRD characterization procedure was applied to analyze the crystallinity, phase purity, and crystal structure of the as-

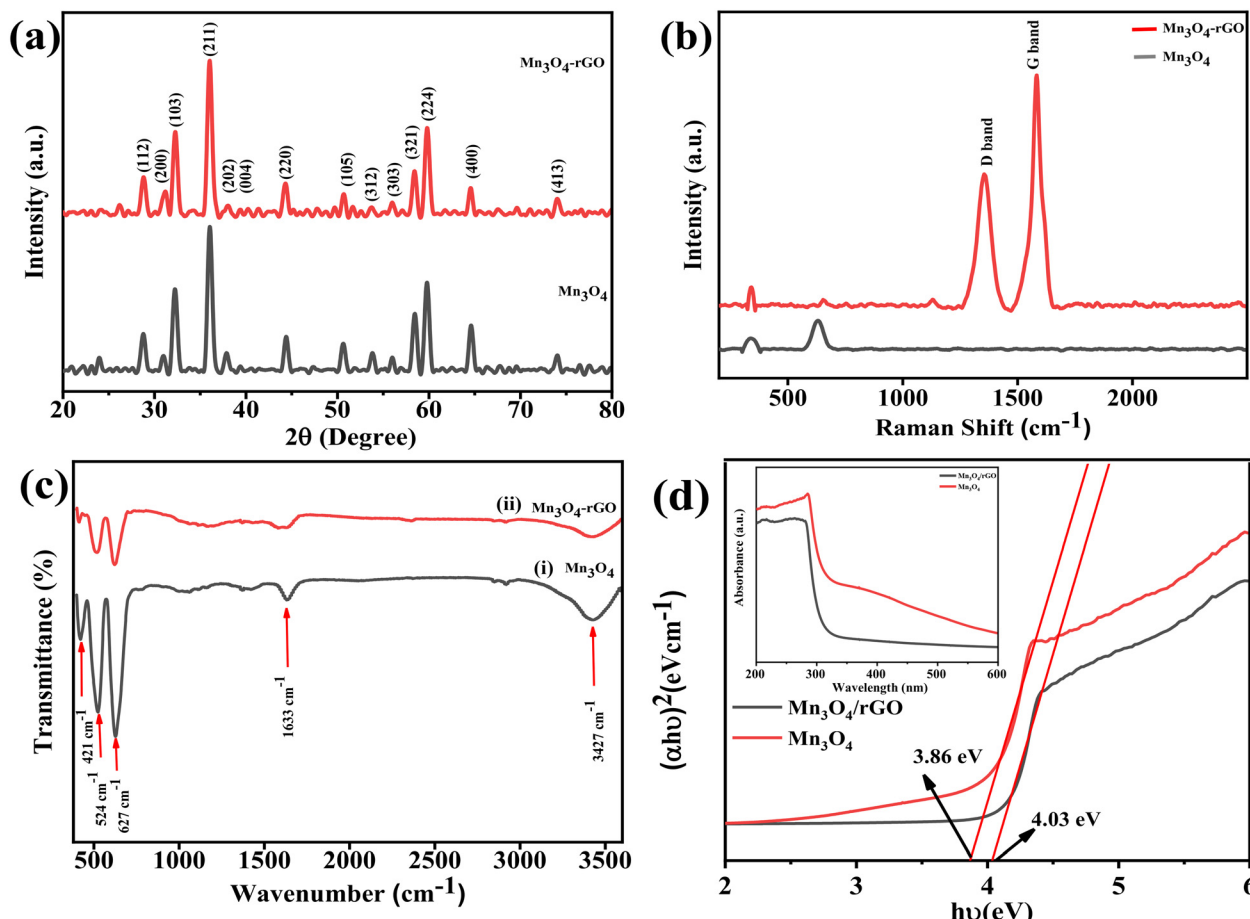


**Fig. 1** (a) XRD, (b) Raman, (c) FTIR, and (d) UV spectra of the as-synthesized Mn<sub>3</sub>O<sub>4</sub> NMs and Mn<sub>3</sub>O<sub>4</sub>/rGO NCs.



synthesized  $\text{Mn}_3\text{O}_4$  NMs and  $\text{Mn}_3\text{O}_4/\text{rGO}$  NCs. The XRD stretches displayed in Fig. 1(a) depict the successful formation of tetragonal spinel-shaped  $\text{Mn}_3\text{O}_4$ , which matches well with JCPDS card No. 24-0734. The Miller indices, along with the corresponding  $2\theta$  angle of all the atomic diffracting planes of the synthesized  $\text{Mn}_3\text{O}_4$  NMs and  $\text{Mn}_3\text{O}_4/\text{rGO}$  NCs, are presented in Fig. 1(a). The XRD diffraction peak of  $\text{Mn}_3\text{O}_4/\text{rGO}$  NCs shows no additional peak of rGO; this may be possibly due to its amorphous nature and nucleation and growth of the  $\text{Mn}_3\text{O}_4$  NMs throughout the surface of rGO, impeding its degree of graphitization.<sup>34</sup> However, a minor variation in the full-width at half-maxima (FWHM) and crystallinity of the  $\text{Mn}_3\text{O}_4/\text{rGO}$  NCs is remarked as associated with the  $\text{Mn}_3\text{O}_4$  NMs, validating the synthesis of  $\text{Mn}_3\text{O}_4/\text{rGO}$  NCs. The addition of rGO has slightly hampered the growth of  $\text{Mn}_3\text{O}_4$  NMs along the respective favored directions, due to which the crystallinity of the  $\text{Mn}_3\text{O}_4/\text{rGO}$  becomes compromised, and a minor widening in FWHM of the characteristic peak is noted. The average crystallite size ( $D$ ) of the as-synthesized materials was determined by putting FWHM ( $\beta$ ) and  $2\theta$  values in the Scherrer equation, as presented in eqn (1):

$$D = \frac{K\lambda}{\beta \cos\theta} \quad (1)$$

Here  $K$  ( $= 0.9$ ) is the shape factor, and  $\lambda$  ( $= 1.54 \text{ \AA}$ ) is the X-ray source wavelength. To calculate  $D$ , the  $\beta$  value was obtained by fitting the XRD peaks to the Gaussian function. The estimated value of average crystallite size for the  $\text{Mn}_3\text{O}_4$  NMs and  $\text{Mn}_3\text{O}_4/\text{rGO}$  NCs was  $18.1 \text{ nm}$  and  $17.3 \text{ nm}$ , respectively [XRD spectra of GO and rGO are mentioned in the SI manuscript as Fig. S1(a)].

### 3.2. FTIR study

The chemical characterization of the as-synthesized  $\text{Mn}_3\text{O}_4$  NMs and  $\text{Mn}_3\text{O}_4/\text{rGO}$  NCs has been explored through FTIR techniques, as represented in Fig. 1(c). The FTIR spectra of  $\text{Mn}_3\text{O}_4$  NMs and  $\text{Mn}_3\text{O}_4/\text{rGO}$  NCs, as displayed in Fig. 1(c), (i), and (ii), display all three signature bands of  $\text{Mn}_3\text{O}_4$  NMs at  $421 \text{ cm}^{-1}$ ,  $524 \text{ cm}^{-1}$ , and  $627 \text{ cm}^{-1}$ . The band at  $627 \text{ cm}^{-1}$  corresponds to the Mn–O stretching vibration in tetrahedral sites, and the band at  $524 \text{ cm}^{-1}$  can be allocated to the distorted vibration in the octahedral sites. Moreover, the  $421 \text{ cm}^{-1}$  band represents the  $\text{Mn}^{3+}$  species vibration in the octahedral sites.<sup>35</sup> The band at  $1633 \text{ cm}^{-1}$  and  $3427 \text{ cm}^{-1}$  suggests the bending and stretching of O–H bands. In the  $\text{Mn}_3\text{O}_4/\text{rGO}$  NCs, there is no significant peak of a functional group containing oxygen observed, suggesting the effective mitigation of GO to rGO [FTIR spectra of GO and rGO are mentioned in the SI manuscript as Fig. S1(c)].

### 3.3. Raman study

The  $\text{Mn}_3\text{O}_4$  NM and  $\text{Mn}_3\text{O}_4/\text{rGO}$  NC Raman spectra are described in Fig. 1(b). It shows that in the Raman spectrum of  $\text{Mn}_3\text{O}_4$  NMs, the peak detected at  $652 \text{ cm}^{-1}$  resembles the

$\text{A}_{1g}$  vibration mode, arising due to the Mn–O bending vibration of the tetrahedrally coordinated  $\text{Mn}^{2+}$  ion in the spinel structure of  $\text{Mn}_3\text{O}_4$  NMs.<sup>36</sup> Another peak at  $366 \text{ cm}^{-1}$  is assigned to the linked vibration of the  $\text{O}^{2-}$  ions that are arranged tetragonally and hexagonally in the spinel structure.<sup>37</sup> Furthermore, for  $\text{Mn}_3\text{O}_4/\text{rGO}$  NCs, the peaks at  $1352 \text{ cm}^{-1}$  and  $1588 \text{ cm}^{-1}$  resemble the D band and G band of rGO, which confirms the synthesis of  $\text{Mn}_3\text{O}_4/\text{rGO}$  NCs.<sup>38,39</sup> The D band denotes the defect and disorder in the rGO structure and arises as a result of the out-of-plane vibrations of the  $\text{sp}^2$  carbon atoms.<sup>34,40</sup> Consequently, the G band signifies the graphitic nature and is ascribed to the in-plane vibration of the  $\text{sp}^2$  carbon atoms. The  $I_D/I_G$  ratios for the  $\text{Mn}_3\text{O}_4/\text{rGO}$  NCs were observed to be increased as compared to the pristine rGO. The increment in the  $I_D/I_G$  ratios of  $\text{Mn}_3\text{O}_4/\text{rGO}$  NCs as compared to the pure rGO suggests the interaction between  $\text{Mn}_3\text{O}_4$  NMs and rGO.<sup>41,42</sup> Additionally, the blue shift of the  $\text{Mn}_3\text{O}_4$  NM peaks in  $\text{Mn}_3\text{O}_4/\text{rGO}$  NCs is evident, which is assigned to the formation of a metal oxide–carbon bond [Raman spectra of GO and rGO are mentioned in the SI manuscript as Fig. S1(b)].

### 3.4. UV-visible study

A UV-visible spectrometer was employed to scrutinize the optical properties of the as-synthesized pristine  $\text{Mn}_3\text{O}_4$  NMs and  $\text{Mn}_3\text{O}_4/\text{rGO}$  NCs. Fig. 1(d) exhibits the optical band gap energies of the as-synthesized  $\text{Mn}_3\text{O}_4$  NMs and  $\text{Mn}_3\text{O}_4/\text{rGO}$  NCs with the inset absorption spectra. It is apparent from the UV-visible spectrum of  $\text{Mn}_3\text{O}_4$  NMs that absorption peaks are observed at  $287 \text{ nm}$  and  $400 \text{ nm}$ . These absorption peaks are attributed to charge transfer between  $\text{O}^{2-}$  to  $\text{Mn}^{2+}$  and  $\text{O}^{2-}$  to  $\text{Mn}^{3+}$ .<sup>43–45</sup> However, in the  $\text{Mn}_3\text{O}_4/\text{rGO}$  NCs, the absorption peak was distinguished at  $280 \text{ nm}$ , showing a blue shift as related to the pristine sample, suggesting interaction between rGO and  $\text{Mn}_3\text{O}_4$  NMs. The optical absorption analysis of the synthesized NMs revealed a certain basic absorption edge that follows Tauc's relation for permitted direct transition. Additionally, a decrease in the particle size of  $\text{Mn}_3\text{O}_4$  NMs was observed to increase the optical band gap ( $E_g$ ).

The band gap of the  $\text{Mn}_3\text{O}_4$  NMs and  $\text{Mn}_3\text{O}_4/\text{rGO}$  NCs was evaluated by employing Tauc's relation given in eqn (2).

$$(\alpha h\nu)^n = K(h\nu - E_g) \quad (2)$$

Here,  $\alpha$  is the coefficient of absorption,  $h\nu$  represents the energy of a photon,  $E_g$  is the band gap,  $k$  is a constant, and the value of  $n$  represents allowed and forbidden transitions, respectively. For direct and indirect allowed transitions, the value of  $n$  is 2 and  $1/2$ . The  $\text{Mn}_3\text{O}_4$  NMs and  $\text{Mn}_3\text{O}_4/\text{rGO}$  NCs show a direct band gap, and their energy for the band gap was calculated by extending the linear portion of the graph between  $(\alpha h\nu)^2$  and  $h\nu$ , as exhibited in Fig. 1(d). The calculated energy band gap for  $\text{Mn}_3\text{O}_4$  NMs and  $\text{Mn}_3\text{O}_4/\text{rGO}$  NCs is  $3.86 \text{ eV}$  and  $4.03 \text{ eV}$ .



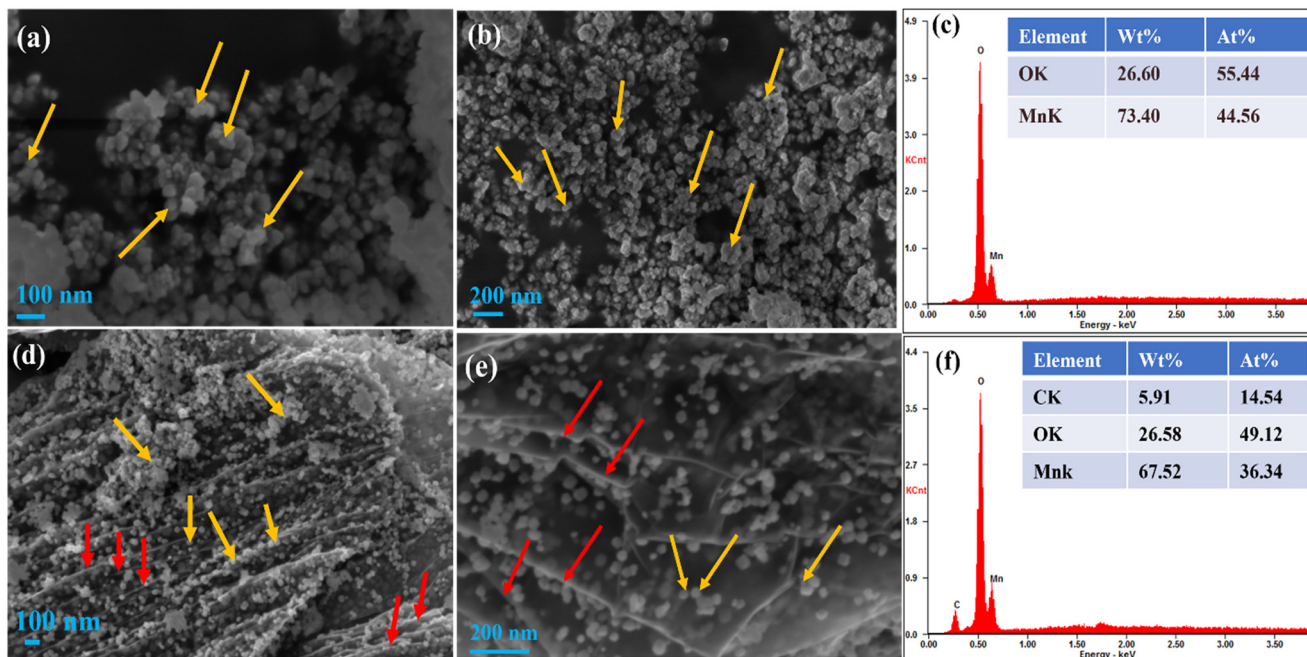


Fig. 2 (a and b) SEM images of  $\text{Mn}_3\text{O}_4$  NMs, (c) EDS energy spectrum of  $\text{Mn}_3\text{O}_4$  NMs, (d and e) SEM image of  $\text{Mn}_3\text{O}_4$ /rGO NCs, (f) EDS energy spectrum of  $\text{Mn}_3\text{O}_4$ /rGO NCs.

### 3.5. Morphology study

The SEM descriptions of  $\text{Mn}_3\text{O}_4$  NMs are displayed in Fig. 2(a and b) at diverse magnifications, which show the agglomerated spherical morphology of  $\text{Mn}_3\text{O}_4$  NMs, indicated *via* the yellow arrows, and Fig. 2(c) exhibits the corresponding EDS energy spectrum of the synthesized  $\text{Mn}_3\text{O}_4$  NMs, which exhibits the occurrence of Mn and O only in the atomic ratio of 3:4.  $\text{Mn}_3\text{O}_4$ /rGO NCs SEM images are presented in Fig. 2(d and e) at diverse amplification in which we obtain the self-assembling  $\text{Mn}_3\text{O}_4$  NMs (indicated *via* yellow arrows) and suggest the even distribution of spherical  $\text{Mn}_3\text{O}_4$  NMs on the surface of rGO; the rGO layer is indicated *via* red arrows. In Fig. 2(f), the corresponding EDS energy plot of the synthesized  $\text{Mn}_3\text{O}_4$ /rGO NCs suggests the coexistence of Mn, O, and C elements. The curved rGO surface specifies the elimination of the usual oxygen-bearing functional group [SEM image of GO and rGO mentioned in the SI manuscript as Fig. S2(b) and (e), and EDAX spectra of GO and rGO mentioned in the SI manuscript as Fig. S2(c) and (f)].

Fig. 3(a and b) demonstrates the TEM image of  $\text{Mn}_3\text{O}_4$  NMs, further confirming its spherical morphology, and the particle size histogram inset in Fig. 3(a) shows an average particle size of 44 nm. Fig. 3(c) shows the HR-TEM representation of the  $\text{Mn}_3\text{O}_4$  NMs, and its zoom version is shown in Fig. 3(g), having an interplanar distance of 0.29 nm, consistent with the (200) plane. Fig. 3(d) exemplifies the selected area electron diffraction (SAED) arrangement, specifying the well-crystalline features of the  $\text{Mn}_3\text{O}_4$  NMs. Fig. 3(e and f) represents a highly crystalline and well-

ordered atomic arrangement of the  $\text{Mn}_3\text{O}_4$  NMs. Fig. 3(h) exhibits the TEM image of the  $\text{Mn}_3\text{O}_4$ /rGO NCs; in Fig. 3(i), it is visible that  $\text{Mn}_3\text{O}_4$  NMs are uniformly dispersed and well anchored on the rGO surface particle, and the particle size histogram shows an average particle size of 44 nm. Fig. 3(j) exhibits the HR-TEM portrait of the  $\text{Mn}_3\text{O}_4$ /rGO NCs, and its zoom version is shown in Fig. 3(n), having an interplanar distance of 0.20 nm, consistent with the (220) plane. Fig. 3(k) illustrates the SAED figure that recommends the good crystalline characteristics of the  $\text{Mn}_3\text{O}_4$ /rGO NCs. This is further validated *via* Fig. 3(l and m), which represents a highly crystalline and well-ordered atomic arrangement of the  $\text{Mn}_3\text{O}_4$ /rGO NCs. The SAED pattern of the  $\text{Mn}_3\text{O}_4$ /rGO NCs suggests that the crystallinity of the  $\text{Mn}_3\text{O}_4$  NMs has not been hampered after the introduction of rGO, which further validates the XRD spectrum [TEM image of GO and rGO mentioned in the SI manuscript as Fig. S2(a) and (d)].

### 3.6. XPS

XPS techniques have been employed to study the elemental constitution, oxidation states, and chemical states of the atoms within the as-synthesized  $\text{Mn}_3\text{O}_4$  NMs and  $\text{Mn}_3\text{O}_4$ /rGO NCs, as exposed in Fig. 4. The survey spectra of  $\text{Mn}_3\text{O}_4$  NMs and  $\text{Mn}_3\text{O}_4$ /rGO NCs exhibited in Fig. 4(a) show the existence of elements Mn, C, and O in both  $\text{Mn}_3\text{O}_4$  and  $\text{Mn}_3\text{O}_4$ /rGO. Fig. 4(b) and (c) show the high-resolution (HR) XPS spectra of Mn 2p in  $\text{Mn}_3\text{O}_4$  NMs and  $\text{Mn}_3\text{O}_4$ /rGO NCs, respectively. The Mn 2p<sub>3/2</sub> and Mn 2p<sub>1/2</sub> peaks of the Mn 2p orbital in both the  $\text{Mn}_3\text{O}_4$  NMs and the  $\text{Mn}_3\text{O}_4$ /rGO NCs are deconvoluted



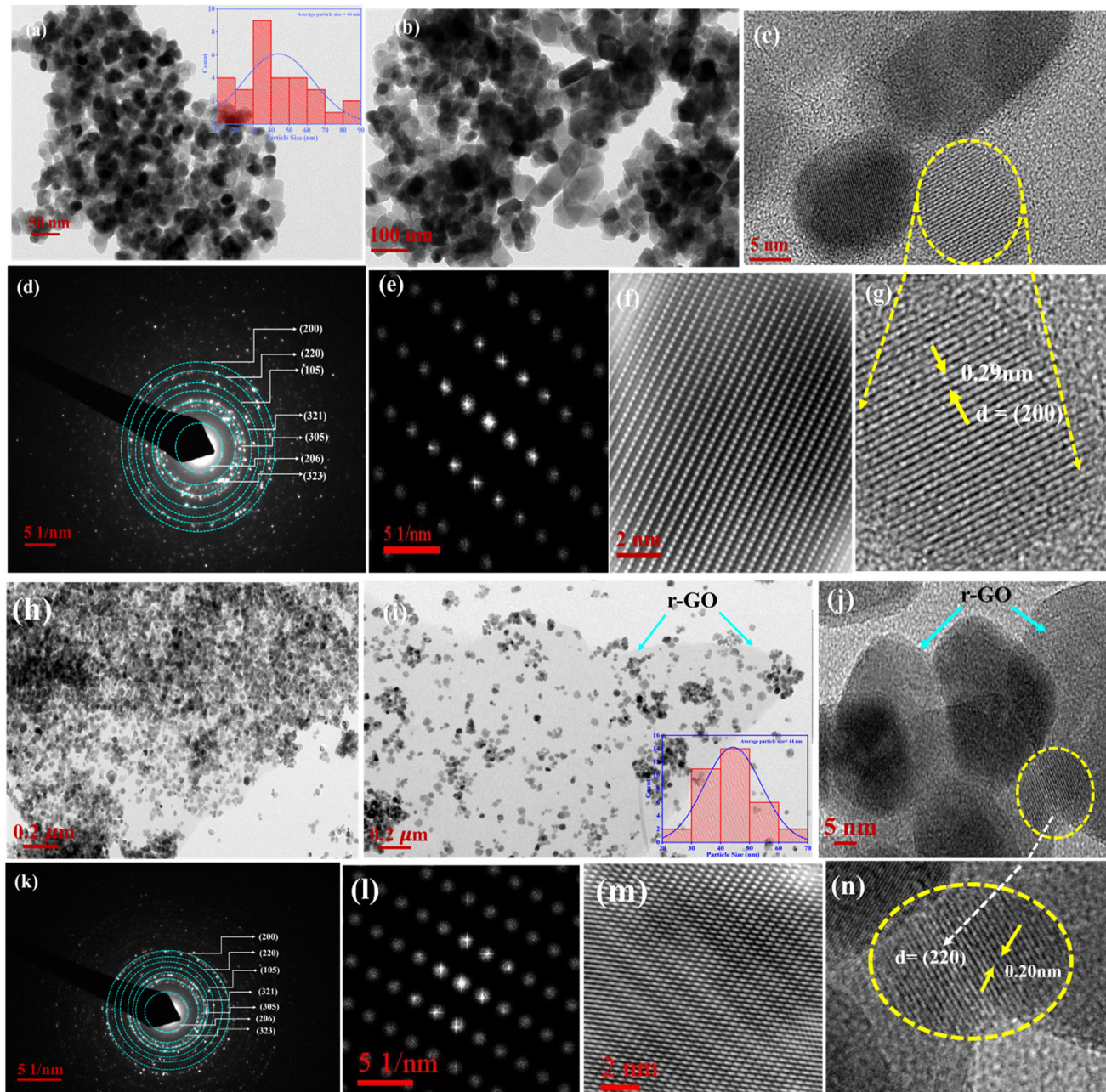


**Fig. 3** (a) TEM image of the  $\text{Mn}_3\text{O}_4$  NMs with an inset of the TEM histogram. (b) TEM image of the  $\text{Mn}_3\text{O}_4$  NMs (100 nm). (c) TEM image of  $\text{Mn}_3\text{O}_4$  NMs showing fringes. (d and e) SAED pattern of  $\text{Mn}_3\text{O}_4$  NMs validating different planes. (f) FFT image of  $\text{Mn}_3\text{O}_4$  NMs. (g) Zoomed TEM image of (c) showing the interplanar distance within  $\text{Mn}_3\text{O}_4$  NMs. (h and i) TEM images of  $\text{Mn}_3\text{O}_4$ /rGO NCs, which show that the  $\text{Mn}_3\text{O}_4$  NMs are scattered on the sheet of rGO (indicated via blue arrows), also with an inset of the TEM histogram. (j) HR-TEM image of  $\text{Mn}_3\text{O}_4$ /rGO NCs. (k and l) SAED pattern of  $\text{Mn}_3\text{O}_4$ /rGO NCs representing different planes. (m) FFT image of  $\text{Mn}_3\text{O}_4$ /rGO NCs. (n) Zoomed TEM image of (j) showing interplanar distance within  $\text{Mn}_3\text{O}_4$ /rGO NCs.

into two peaks. In  $\text{Mn}_3\text{O}_4$  NMs, binding energies 642.8 eV and 643.9 eV belong to the two deconvoluted peaks of Mn 2p<sub>3/2</sub>, and binding energies 654.3 eV and 655.3 eV are associated with the two deconvoluted peaks of Mn 2p<sub>1/2</sub> (Fig. 4b). Similarly, for the  $\text{Mn}_3\text{O}_4$ /rGO NCs, binding energies 642.4 eV and 643.7 eV correspond to the two deconvoluted peaks of Mn 2p<sub>3/2</sub>, and binding energies 654.2 eV and 655.4 eV resemble the two deconvoluted peaks of Mn 2p<sub>1/2</sub> (ref. 46).

and 47) (Fig. 4c). The existence of the two additional peaks within the two peaks of Mn 2p<sub>3/2</sub> and Mn 2p<sub>1/2</sub> of the Mn 2p orbital suggests the occurrence of two oxidation states,  $\text{Mn}^{3+}$  and  $\text{Mn}^{2+}$ , of Mn for all  $\text{Mn}_3\text{O}_4$  present in  $\text{Mn}_3\text{O}_4$  NMs and  $\text{Mn}_3\text{O}_4$ /rGO NCs, respectively. Furthermore, in the  $\text{Mn}_3\text{O}_4$  NMs and  $\text{Mn}_3\text{O}_4$ /rGO NCs, the calculated energy gaps among the Mn 2p<sub>3/2</sub> and Mn 2p<sub>1/2</sub> were 11.8 eV and 11.7 eV, respectively. The slightly lower energy gap in

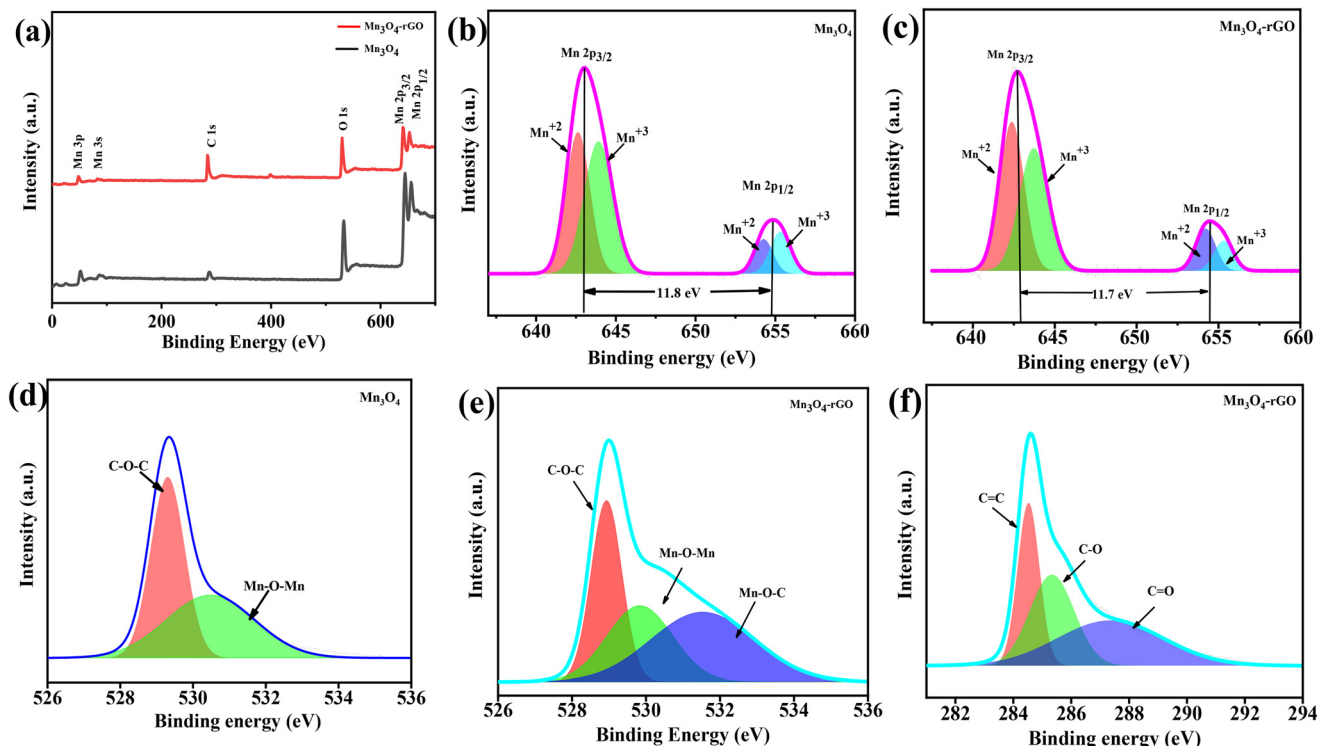


Fig. 4 (a) Survey spectrum, (b and c) HR Mn 2p spectra, (d and e) HR Mn O 1s spectrum of  $\text{Mn}_3\text{O}_4$  NMs and  $\text{Mn}_3\text{O}_4$ /rGO NCs, and (f) HR Mn C 1s spectrum of  $\text{Mn}_3\text{O}_4$ /rGO NMs.

$\text{Mn}_3\text{O}_4$ /rGO NCs signifies the interactions of  $\text{Mn}_3\text{O}_4$  NMs and rGO.<sup>47–49</sup> Fig. 4(d) and (e) depict the HR O 1s spectrum of  $\text{Mn}_3\text{O}_4$  and  $\text{Mn}_3\text{O}_4$ /rGO. The O 1s spectrum of  $\text{Mn}_3\text{O}_4$  NMs comprises two deconvoluted peaks at 529.1 eV and 530.4 eV, which correspond to the binding energy of C–O–C and Mn–O–Mn (Fig. 4(d)). For the  $\text{Mn}_3\text{O}_4$ /rGO NCs, the O 1s spectra comprise triple deconvoluted peaks at 529.9 eV, 529.8 eV, and 531.6 eV ascribed to C–O–C, Mn–O–Mn, and Mn–O–C, demonstrating the mutual existence of Mn, C, and O in the  $\text{Mn}_3\text{O}_4$ /rGO NCs.<sup>50</sup> The HR C 1s spectra of  $\text{Mn}_3\text{O}_4$ /rGO NCs displayed in Fig. 4(f) possess three deconvoluted peaks at 284.5 eV, 285.3 eV, and 287.6 eV, referred to C=C, C–O, and C=O of rGO in the  $\text{Mn}_3\text{O}_4$ /rGO NCs.<sup>50</sup>

#### 4. Photodegradation of MB dye

MB was used as a model dye to test how well the synthesized  $\text{Mn}_3\text{O}_4$  NMs and  $\text{Mn}_3\text{O}_4$ /rGO NCs could break down contaminants under UV light. For this experiment, a 20 ppm solution of the dye was prepared. Then, 30 mg of the catalyst was mixed into 30 mL of this dye solution. This solution was mixed continuously in the dark for 60 minutes to allow the MB dye and the photocatalyst to reach a stable adsorption–desorption state. After this initial phase, the solution was exposed to UV light to monitor how effectively the dye was broken down in the proximity of the photocatalyst. Throughout the experiment,  $\text{Mn}_3\text{O}_4$  NMs and  $\text{Mn}_3\text{O}_4$ /rGO NCs of about 3 mL were

taken from the dye solution after every 10 minutes using a micropipette to track the progress of the degradation process. Next, the mixture was centrifuged to isolate and remove the solid particles from the liquid. The clear liquid, or supernatant, was then removed for analysis. The concentration of MB in the samples was measured over time using a UV-vis spectrophotometer (SHIMADZU, 1900i). The optical density was specifically monitored at a wavelength of 664 nm, which corresponds to the characteristic peak of MB, to determine how much dye remained in the solution. Fig. 5(a) and (b) in the study show how the synthesized catalysts,  $\text{Mn}_3\text{O}_4$  NMs and  $\text{Mn}_3\text{O}_4$ /rGO NCs, degrade MB dye under UV light over time. The magnitude of the absorption peak at 664 nm, characteristic of MB, was observed to decrease. The most significant drop in this absorption intensity occurred within 80 minutes when using the  $\text{Mn}_3\text{O}_4$ /rGO NC catalyst. Fig. 5(c) illustrates the correlation between the degradation rate ( $C/C_0$ ) and the irradiation time for MB in the proximity of catalysts  $\text{Mn}_3\text{O}_4$  NMs and  $\text{Mn}_3\text{O}_4$ /rGO NCs, where  $C$  is the dye concentration at a given time and  $C_0$  is the initial concentration. This figure clearly shows that the  $\text{Mn}_3\text{O}_4$ /rGO NC catalyst has the highest degradation rate, while the  $\text{Mn}_3\text{O}_4$  NMs show minute degradation.

The rate constant ( $k$ ) for the degradation procedure using the synthesized catalysts was determined from pseudo-first-order kinetic plots. The rate constant values were evaluated from eqn (3):



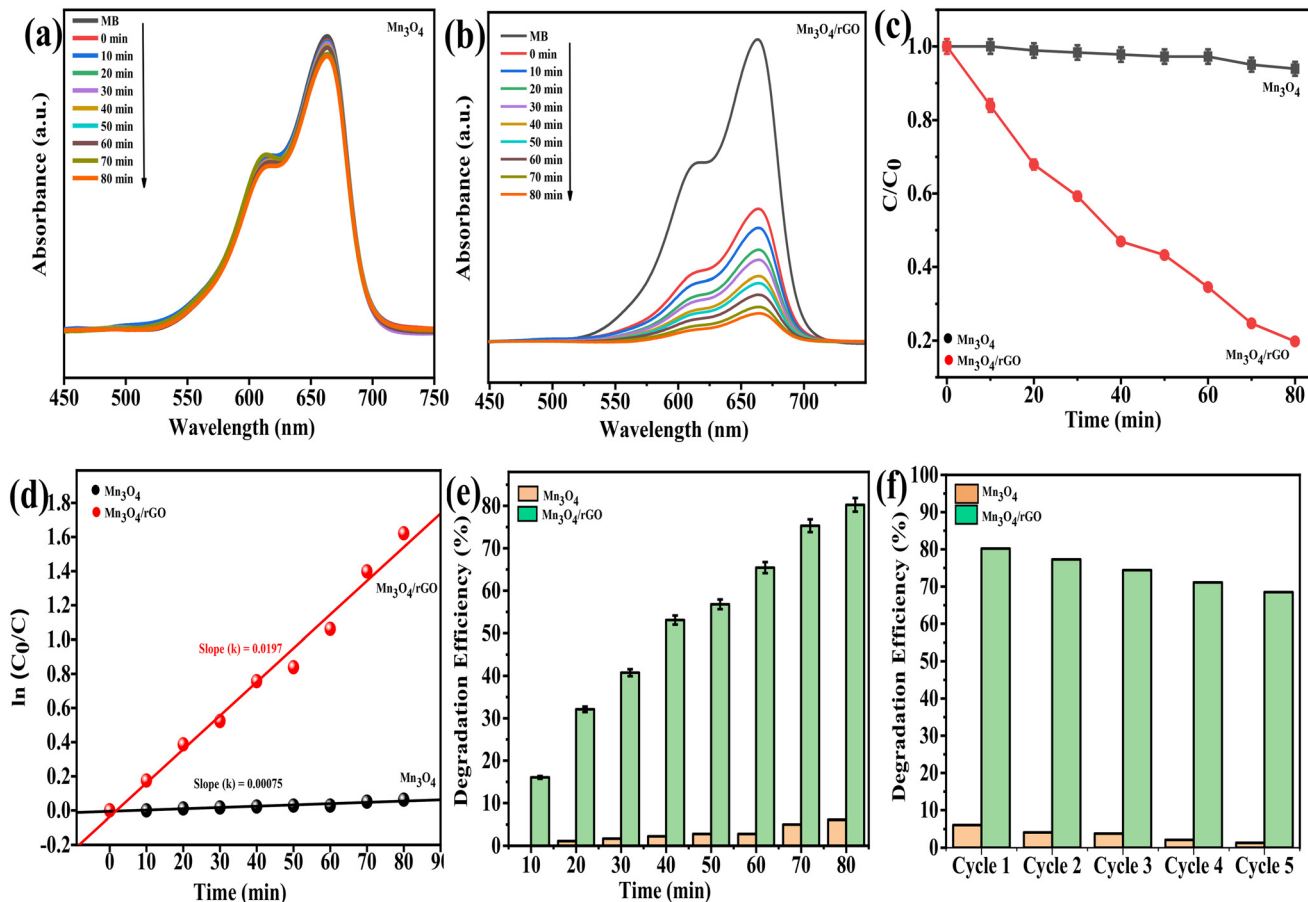


**Fig. 5** (a and b) Absorption spectra showing the breakdown of MB in the presence of Mn<sub>3</sub>O<sub>4</sub> NMs and Mn<sub>3</sub>O<sub>4</sub>/rGO NCs, (c) analysis of the degradation rate, (d) pseudo-first-order kinetics for the reaction, (e) efficiency of dye degradation, and (f) reusability test for the Mn<sub>3</sub>O<sub>4</sub> NM and Mn<sub>3</sub>O<sub>4</sub>/rGO NC catalysts.

$$\ln\left(\frac{C_0}{C}\right) = kt \quad (3)$$

Here,  $k$  is the rate constant, which is derived from the slope of the plot between  $\ln\left(\frac{C_0}{C}\right)$  and time  $t$ , as displayed in Fig. 5(d). The rate constants for the Mn<sub>3</sub>O<sub>4</sub> NMs and Mn<sub>3</sub>O<sub>4</sub>/rGO NCs are 0.00075 and 0.0197, respectively. The significant increase in the rate constant for the Mn<sub>3</sub>O<sub>4</sub>/rGO NCs suggests a considerable improvement in its photocatalytic efficiency.

The efficiency for degradation of the catalyst can be deliberated *via* employing the formula as in eqn (4):

$$\text{Degradation efficiency (\%)} = \left( \frac{C_0 - C}{C_0} \right) \times 100 \quad (4)$$

where  $C_0$  is the dye's initial concentration and  $C$  is the dye concentration at a given time. As shown in Fig. 5(e), the MB dye degradation reached up to 6% with the Mn<sub>3</sub>O<sub>4</sub> NM catalyst and up to 80% with the Mn<sub>3</sub>O<sub>4</sub>/rGO NC catalyst when exposed to UV light for 80 minutes (photodegradation of rGO in the SI section 3.1. and Fig. S3). For a photocatalyst to be practical, it must be reusable and stable. To evaluate this, a

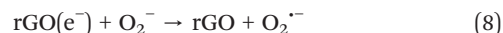
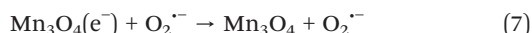
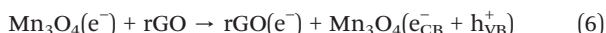
reusability test was performed over five cycles, where the same catalysts were used repeatedly for each cycle. The degradation efficiency was measured after each cycle, as illustrated in Fig. 5(f), which showed that the Mn<sub>3</sub>O<sub>4</sub>/rGO NCs maintained better stability and performance than the Mn<sub>3</sub>O<sub>4</sub> NMs.

#### 4.1. Photodegradation mechanism

When exposed to UV light, the Mn<sub>3</sub>O<sub>4</sub> NMs catalyst loaded onto the rGO surface creates photogenerated holes ( $h^+$ ) in the valence band (VB) and electrons ( $e^-$ ) in the conduction band (CB). In the Mn<sub>3</sub>O<sub>4</sub>-rGO system, rGO functions as an electron acceptor, capturing these photogenerated electrons and greatly enhancing the separation of charges. The pristine Mn<sub>3</sub>O<sub>4</sub> exhibits poor degradation efficiency, having a vast energy band gap and quick recombination of photogenerated  $e^-/h^+$  pairs. However, the Mn<sub>3</sub>O<sub>4</sub>/rGO NC catalyst shows enhanced degradation of the MB dye, possibly due to three main reasons: (i) the high surface area of rGO facilitates more adsorption of MB molecules, (ii) the  $\pi-\pi$  interaction of the positively charged MB dye molecules accompanied by

the oxygenated functioning group on the rGO surface, leading to interaction with more MB molecules in the vicinity of  $\text{Mn}_3\text{O}_4$  NMs and rGO, and (iii) the better conductivity and transport property of rGO facilitate efficient transport of photogenerated electrons in  $\text{Mn}_3\text{O}_4$  NMs, causing delayed electron–hole recombination.

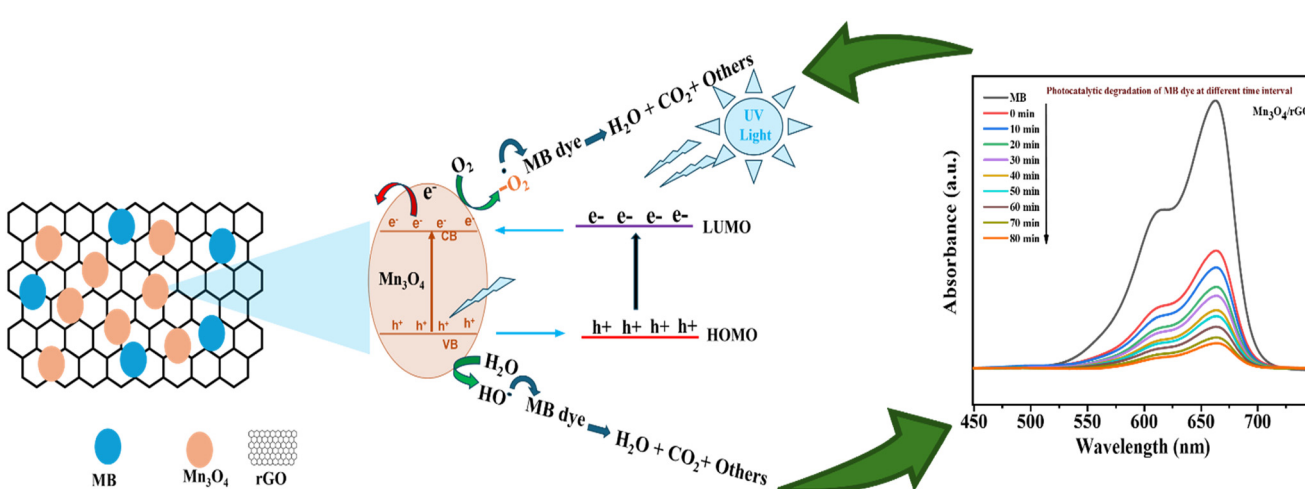
Further, in the  $\text{Mn}_3\text{O}_4$ /rGO NCs, the photogenerated holes and electrons move to different locations on the surface, resulting in the generation of superoxide anions ( $\text{O}_2^{\cdot-}$ ) and hydroxyl radicals ( $\cdot\text{OH}$ ), respectively. Additionally, the result of a scavenger study suggests that upon UV light illumination, the photocatalyst produces conduction band electrons ( $e^-$ ) and valence band holes ( $h^+$ ). The  $e^-$  quickly converts dissolved  $\text{O}_2$  to  $\cdot\text{O}_2^-$ , which starts the major degradation pathway. Superoxide may be protonated to  $\text{HO}_2^-$ , undergo disproportionation/reduction reactions that give  $\text{H}_2\text{O}_2$ , followed by one-electron reduction or photolysis of  $\text{H}_2\text{O}_2$  to yield  $\cdot\text{OH}$ , which continues to oxidize MB and its intermediates. Formation of  $\cdot\text{OH}$  directly from reaction of  $h^+$  with surface  $\text{H}_2\text{O}/\text{OH}^-$  is feasible but occurs to a smaller extent, as seen with only moderate inhibition by IPA. Since EDTA trapping of holes is not activity-reducing, MB direct  $h^+$  oxidation is negligible. Overall, MB degradation occurs principally through an electron-mediated  $\text{O}_2$  activation pathway ( $\text{O}_2^{\cdot-}$ -driven) supplemented by downstream  $\cdot\text{OH}$  attack, leading to stepwise *N*-demethylation, ring opening, and final mineralization to lower inorganic products. Thus, these reactive species ( $\text{O}_2^{\cdot-}$  and  $\cdot\text{OH}$ ) play a key role in breaking down MB during photodegradation. The degradation of MB dye by the  $\text{Mn}_3\text{O}_4$ /rGO NC catalyst in the presence of UV light is shown in Scheme 3 and summarized in eqn (5)–(12).



#### 4.2. Photocatalytic scavenging study

In the entrapping analysis, three distinct scavengers are employed to ascertain the functioning species throughout the photocatalytic degradation of MB dye: EDTA-2Na to entrap photogenerated holes ( $h^+$ ), isopropanol (IPA) to quench hydroxyl radicals ( $\cdot\text{OH}$ ), and *p*-benzoquinone (*p*-BQ) to scavenge superoxide anion radicals ( $\text{O}_2^{\cdot-}$ ). The scavenger tests in dye degradation elucidate to us the reactive species involved in the procedure. The entrapping demonstration was operated under identical environments to the photocatalytic experiments, except that pure MB aqueous solution was substituted with a mixed MB aqueous solution of 10 mM IPA, 10 mM EDTA-2NA, and 10 mM *p*-BQ solution in ethanol.

The optical spectra of the dye degradation procedure in the proximity of scavengers are presented in SI Fig. S4(a–d). The addition of *p*-BQ to the reaction system notably obstructs the catalytic activity, and the effectiveness of MB breakdown reduces from 80% to 27%, demonstrating that the superoxide anion radicals ( $\text{O}_2^{\cdot-}$ ) are the most influential species here. Fig. S4(a) illustrates that the photodegradation of dye is much slower in the proximity of superoxide anion radicals ( $\text{O}_2^{\cdot-}$ ), signifying the active species liable for the oxidative degradation of the dye. Integrating IPA reduces decomposition from 80% to 67%, demonstrating quenching of hydroxyl radicals ( $\cdot\text{OH}$ ) by isopropanol (IPA). Fig. S4(b) illustrates that to some extent, hydroxyl radicals ( $\cdot\text{OH}$ ) are



**Scheme 3** Detailed degradation of MB dye in the presence of  $\text{Mn}_3\text{O}_4$ /rGO NC catalysts.

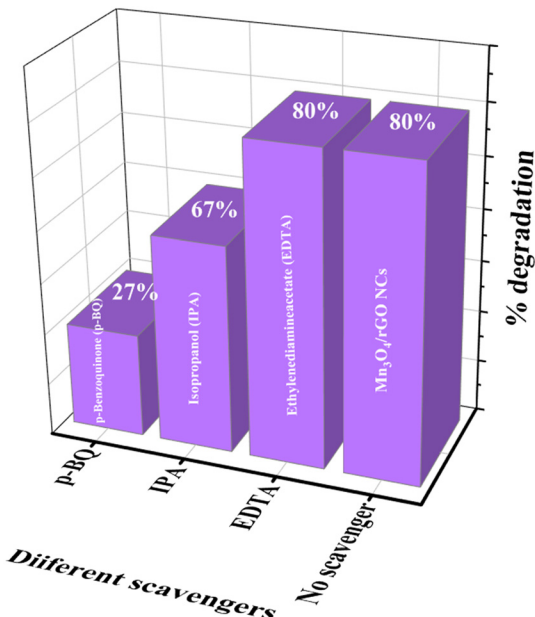


Fig. 6 MB dye degradation with and without scavengers.

also liable for the oxidative degradation of the dye. Fig. S4(c) illustrates that EDTA-2Na decomposition remains identical to that of the Mn<sub>3</sub>O<sub>4</sub>/rGO NCs (from 80% to 80%), which is attributed to a negligible role in the process. The photodegradation of MB is unaffected by the presence of EDTA-2Na in dye solution, signifying that photogenerated holes ( $h^+$ ) do not play a remarkable participation role in its oxidative decomposition, as exhibited in Fig. 6.

## 5. Electrochemical characteristics

### 5.1. Cyclic voltammetry (CV), differential pulse voltammetry (DPV), and electrochemical impedance spectroscopy (EIS) behavior of the modified electrodes

To estimate the conductive nature and electrochemical features of the bare ITO, Mn<sub>3</sub>O<sub>4</sub>/ITO, and Mn<sub>3</sub>O<sub>4</sub>/rGO/ITO, CV and DPV studies of the fabricated electrodes are accomplished in a 0.05 M PBS (0.9% NaCl) solution consisting of 5 mM  $[Fe(CN)_6]^{3-/-4-}$  as a redox couple. The CVs of the bare ITO, Mn<sub>3</sub>O<sub>4</sub>/ITO, and Mn<sub>3</sub>O<sub>4</sub>/rGO/ITO electrodes have an  $I_{pa}$  response of 1.33 mA, 1.325 mA, and 1.393 mA, respectively, as displayed in Fig. 7(a). Such electrochemical characteristics correspond to fine conductivity and a large specific surface area, which collectively propose significant electrocatalytic functioning against bare ITO electrodes, validated by DPV analysis as well. The DPV results of the bare ITO, Mn<sub>3</sub>O<sub>4</sub>/ITO, and Mn<sub>3</sub>O<sub>4</sub>/rGO/ITO electrodes have an  $I_{pa}$  response of 0.46 mA, 0.706 mA, and 0.863 mA, respectively, as displayed in Fig. 7(b). The CVs of the bare ITO, Mn<sub>3</sub>O<sub>4</sub>/ITO, and Mn<sub>3</sub>O<sub>4</sub>/rGO/ITO electrodes have an oxidation/anodic peak current ( $I_{pa}$  response) of 1.33 mA, 1.325 mA, and 1.393 mA, respectively. For the Mn<sub>3</sub>O<sub>4</sub>/rGO/ITO electrode, the  $I_{pa}$  value was higher, having a peak current of 1.393 mA, and for the bare ITO, it was recorded to be 4.7% lower than that of the Mn<sub>3</sub>O<sub>4</sub>/rGO/ITO electrode. There is a 4.7% increase in oxidation current after electrode modification (S. Soylemez *et al.* reported an increase in CV current after modification of 4.84% (ref. 51)).

After modification of ITO with Mn<sub>3</sub>O<sub>4</sub>, there is no significant enhancement in the oxidation/anodic peak

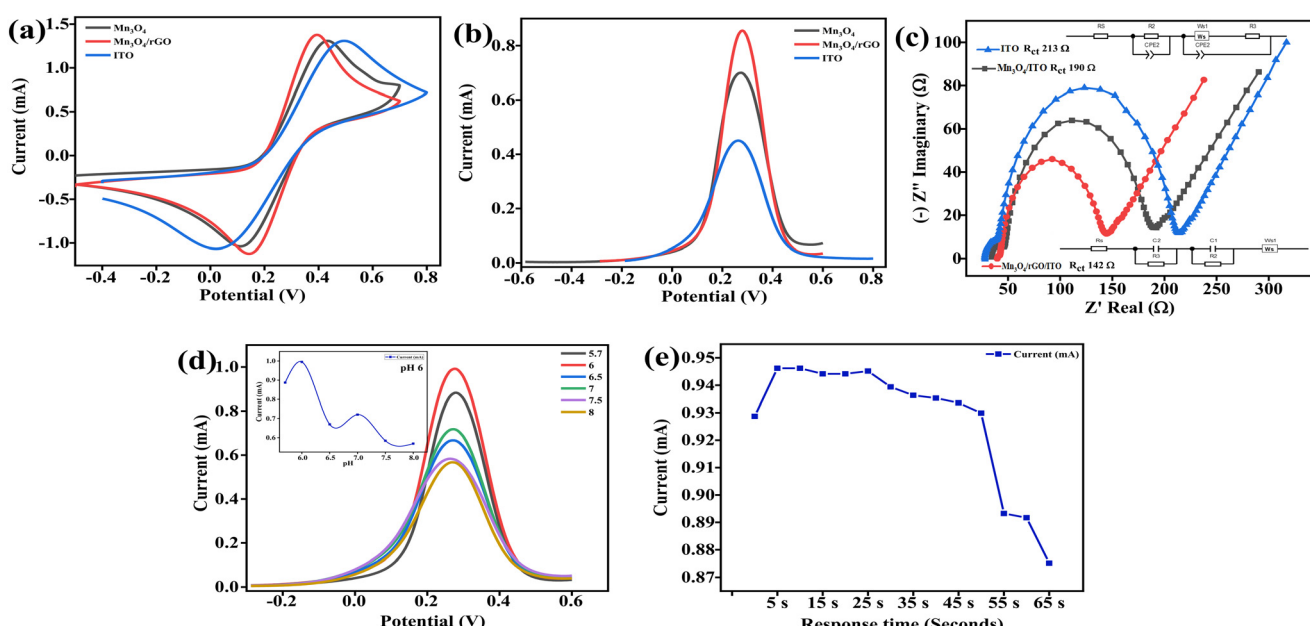


Fig. 7 (a) CV of modified electrodes in PBS containing ferri-/ferrocyanide at  $0.05 V s^{-1}$  scan rate. (b) DPV of various modified electrodes in PBS containing ferri-/ferrocyanide. (c) EIS of various modified electrodes in PBS containing ferri-/ferrocyanide. (d) CV spectrum of Mn<sub>3</sub>O<sub>4</sub>/rGO/ITO at distinct pH (5.7 to 8) PBS with an inset of pH calibration curve. (e) Response time calibration plot of the Mn<sub>3</sub>O<sub>4</sub>/rGO/ITO electrode.

current, which is almost equal to that of the bare electrode. Considering all this, we accomplished that the synthesis of the composite with rGO facilitates better electrical conductivity as compared to the material itself, which is further validated by its increased effective surface area evaluated with the assistance of the Randles–Sevcik equation. The effective surface area of the bare ITO,  $\text{Mn}_3\text{O}_4$ /ITO, and  $\text{Mn}_3\text{O}_4$ /rGO/ITO electrodes is  $1.6 \text{ cm}^2$ ,  $1.595 \text{ cm}^2$ , and  $1.68 \text{ cm}^2$ , respectively. The diffusion coefficient of the redox couple is  $7.6 \times 10^{-6} \text{ cm}^2 \text{ s}^{-1}$ .<sup>52</sup> From here, we can conclude that the electrode modified with the composite has a high surface-active segment for electrochemical sensing. During electrode modification, by means of the EIS study, we found that the estimated  $R_{\text{ct}}$  values for bare ITO,  $\text{Mn}_3\text{O}_4$ /ITO, and  $\text{Mn}_3\text{O}_4$ /rGO/ITO are  $213 \Omega$ ,  $190 \Omega$ , and  $142 \Omega$ , respectively, as represented in Fig. 7(c). We employed the subsequent eqn (13) to estimate the charge transfer rate constant of bare and modified electrodes.<sup>53</sup>

$$K_s = RT/n^2 F^2 A R_{\text{ct}} C \quad (13)$$

Where  $K_s$  is the charge transfer rate constant,  $n$ ,  $R$ ,  $F$ , and  $T$  have their usual meaning,  $A$  is the surface area of the electrode ( $1.68 \text{ cm}^2$ ),  $R_{\text{ct}}$  is the resistance for charge transfer, and  $C$  is the ferri-/ferrocyanide concentration ( $5 \times 10^{-6} \text{ mol cm}^{-3}$ ). The charge transfer rate constants ( $K_s$ ) for the bare ITO,  $\text{Mn}_3\text{O}_4$ /ITO, or  $\text{Mn}_3\text{O}_4$ /rGO/ITO are  $15.2 \Omega$ ,

$17.1 \Omega$ , and  $21.7 \Omega$ , respectively.  $\text{Mn}_3\text{O}_4$ /rGO/ITO displays the lowest resistance ( $R_{\text{ct}}$ ) in comparison to the bare ITO and  $\text{Mn}_3\text{O}_4$ /ITO, and subordinate  $R_{\text{ct}}$  values verify the faster electron transfer mechanism on the  $\text{Mn}_3\text{O}_4$ /rGO/ITO electrode. In electron transfer reactions, an enhanced  $K_s$  entails rapid electron transfer, while a lower  $K_s$  entails slower transfer. Hence, the reaction with high  $K_s$  and lower resistance ( $R_{\text{ct}}$ ) is quicker and more effective in electron transfer. From the CV, DPV, and EIS study of the modified electrode, we found that after modification, an enhancement in current takes place. Consequently, we demonstrate that as we modify the electrode, the electrocatalytic conductance of the operational electrode improves towards the 2,4,6-TCP oxidation process. This happens generally because the modified electrode possesses broader electroactive site content, enhancing increased adsorption on the active surface and the uppermost electron transfer rate, which is appropriate for electrochemical sensing applications.

## 5.2. Optimization of pH of the $\text{Mn}_3\text{O}_4$ /rGO/ITO electrode

The potent essence of pH on the  $I_{\text{pa}}$  response of the analyte was estimated; during pH optimization, the pH range was from 5.7 to 8. During initiation, the  $I_{\text{pa}}$  response of the analyte intensifies from pH 5.7 to 6. Furthermore, as the pH increased from 6.5 to 8, a decrease in the  $I_{\text{pa}}$  response current of the analyte was observed. We found

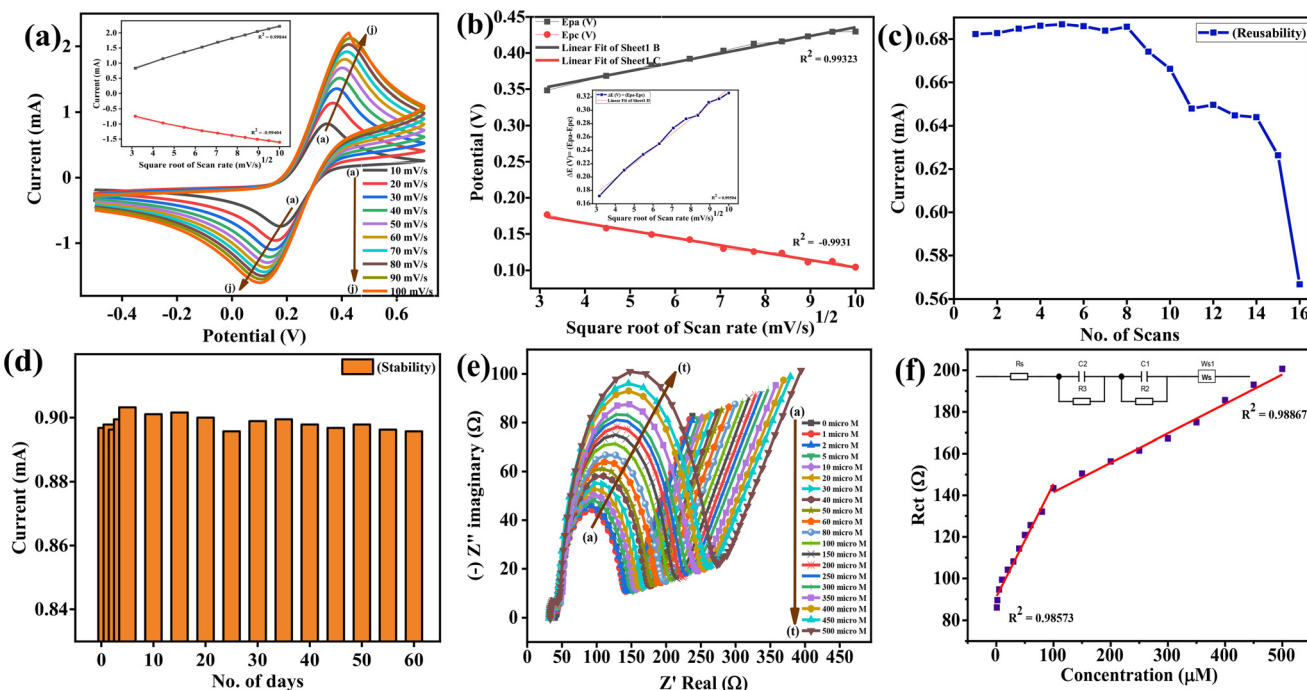


**Fig. 8** (a) CV plot of the scan rate plot extends from  $10$  to  $100 \text{ mV s}^{-1}$  with an inset of the linear calibration curve of the square root of the scan rate vs. anodic and cathodic current (mA). (b) Linear calibration curve of the square root of the scan rate vs. anodic and cathodic potential (V) with an inset of the linear calibration curve of the square root of the scan rate vs. the difference of the anodic and cathodic potential (V). (c) Reusability. (d) Stability plot of the  $\text{Mn}_3\text{O}_4$ /rGO/ITO electrode. (e) Nyquist plot of the 2,4,6-TCP sensing in PBS containing ferri-/ferrocyanide (pH 6) and varying concentrations of 2,4,6-TCP (f). Linear regression plot (with inset of the fitted equivalent circuit) for 2,4,6-TCP ( $\mu\text{M}$ ) concentration vs.  $R_{\text{ct}}$  ( $\Omega$ ).



maximal  $I_{pa}$  current response at pH 6, illustrated in Fig. 7(d). Considering the pH dependency result, pH 6 was picked out as the optimal pH. pH optimization with buffers sustains reliability as well as adjusts redox potential, which is usually crucial in electrochemistry. Hence, it was accomplished that pH 6 functionally supports the confirmation of 2,4,6-TCP, and it was effective for an all-inclusive electrochemical assessment.

### 5.3. Scan rate and kinetics of the $\text{Mn}_3\text{O}_4/\text{rGO/ITO}$ electrode

The scan rate extent was used to study the efficiency and consistency of a  $\text{Mn}_3\text{O}_4/\text{rGO/ITO}$  electrochemical sensor. The electrochemical functioning of the fabricated  $\text{Mn}_3\text{O}_4/\text{rGO/ITO}$  electrode, containing redox operations, heterogeneous electron transfer, and the adsorption process of electroactive species, was estimated *via* CV techniques. The CV spectrum for the  $\text{Mn}_3\text{O}_4/\text{rGO/ITO}$  electrode exhibited in Fig. 8(a) concerns varied scan rates extending from 10 to 100  $\text{mV s}^{-1}$ . A linear affinity between  $I_{pa}$  and  $I_{pc}$  and  $v^{1/2}$  was monitored. The results demonstrate an increment in the oxidation peak current ( $I_{pa}$ ) (positive shifting of potential in anodic peak current) and a decrement in the reduction peak current ( $I_{pc}$ ) (negative shifting of potential in cathodic peak current), accompanied by rising scan rate ( $v$ ) (SI Table S1). The peak-to-peak separation ( $\Delta E_p$ ) is a fundamental variable for estimating the electrochemical characteristics of the sensing constituents. The distinction in the anodic and cathodic peak potential separation ( $\Delta E = E_{pa} - E_{pc}$ ) with the variable scan rates proposed the quasi-reversible nature of an electrochemical technique. Fig. 8(b) shows a scheme that includes straight line fitting displaying the linear reliance of peak current extent on  $v^{1/2}$  (coefficient of regression,  $R^2$  of 0.99844 for  $I_{pa}$  and 0.99404 for  $I_{pc}$ ), thus illustrating the diffusion-controlled redox phenomenon at the electrode-electrolyte edge.<sup>54</sup>

$K_s$  is the rate constant for charge transfer of the electrochemical reaction ( $\text{s}^{-1}$ ) and is derived from the Lavrion model,<sup>55</sup> *i.e.*, eqn (14), mathematically reorganized in eqn (15) to estimate the  $K_s$ .

$$m = (RT/F)(K_s/nv) \quad (14)$$

$$K_s = mnFv/RT \quad (15)$$

Here,  $n$  ( $n = 1$ ) refers to the quantity of electrons transported,  $F$  is the Faraday constant ( $96\,485 \text{ C mol}^{-1}$ ),  $v$  is the scan rate ( $0.05 \text{ V s}^{-1}$ ),  $R$  is the ideal gas constant ( $8.314 \text{ J K}^{-1} \text{ mol}^{-1}$ ), estimating potential variance ( $\Delta E_p = E_{pc} - E_{pa}$ ) at  $0.05 \text{ V s}^{-1}$ ,  $m$  is the separation between peaks, and  $T$  is the temperature ( $300 \text{ K}$ ). By placing the content of all the criteria, the  $K_s$  evaluated for the  $\text{Mn}_3\text{O}_4/\text{rGO/ITO}$  electrode is  $0.53 \text{ s}^{-1}$ .

Concentration at the surface of the  $\text{Mn}_3\text{O}_4/\text{rGO/ITO}$  electrode is feasibly predictable by utilizing the Brown-Anson model,<sup>56</sup> which is predicated on the following eqn (16).

$$I_p = n^2 F^2 \gamma Av / 4RT \quad (16)$$

Here,  $\gamma$  is the surface concentration of the  $\text{Mn}_3\text{O}_4/\text{rGO/ITO}$  electrode ( $\text{mol cm}^{-2}$ ),  $v$  is the scan rate ( $50 \text{ mV s}^{-1}$ ),  $n$ ,  $R$ ,  $F$ , and  $T$  have their usual meaning.  $A$  is the effective electrode's area ( $1.68 \text{ cm}^2$ ). By placing values of all the standards,  $\gamma$  is assessed as  $1.28 \times 10^{-7} \text{ mol cm}^{-2}$ . Further, the Randles-Sevcik eqn (17) illustrates the coefficient of diffusion ( $D$ ) of the  $\text{Mn}_3\text{O}_4/\text{rGO/ITO}$  electrode.

$$I_p = (2.69 \times 10^5) n^{3/2} A C D^{1/2} v^{1/2} \quad (17)$$

where  $A$  is the electrode surface area ( $1.68 \text{ cm}^2$ ),  $C$  is concentration in  $\text{mol cm}^{-3}$ ,  $D$  is the coefficient of diffusion,  $\text{cm}^2 \text{ s}^{-1}$ ,  $I_p$  is the peak current response in  $\text{mA}$ ,  $n$  is denoted as the quantity of electrons involved in a redox reaction (usually 1),  $v$  is the scan rate ( $\text{V s}^{-1}$ ),  $R$  is the gas constant in  $\text{J K}^{-1} \text{ mol}^{-1}$ .  $D$  is estimated as  $7.93 \times 10^{-3} \text{ cm}^2 \text{ s}^{-1}$ .

### 5.4. Response time study of the $\text{Mn}_3\text{O}_4/\text{rGO/ITO}$ electrode

The response time study of the modified  $\text{Mn}_3\text{O}_4/\text{rGO/ITO}$  electrode was evaluated by exposing  $20 \mu\text{L}$  of  $50 \mu\text{M}$  2,4,6-TCP solution to the electrolyte by changing the stretch successively starting from 0 to 60 s (SI Table S2 and Fig. S5(a)). The maximum current response was attained at 5–10 seconds, displayed in Fig. 7(e). Afterward, the current was nearly maintained up to 60 seconds; hence, the perfect reaction time to intercommunicate with 2,4,6-TCP was determined to be 10 seconds.

### 5.5. EIS sensing of the $\text{Mn}_3\text{O}_4/\text{rGO/ITO}$ electrode

EIS is an invaluable tool for examining surface variations on modified electrodes. The EIS spectrum was reported in a  $[\text{Fe}(\text{CN})_6]^{3-/-4-}$  probe. The impedance spectra comprised two chief constituents: a semicircle segment in the higher frequency zone, indicating the electron transfer-limited process, and a linear segment in the low-frequency zone, consistent with the diffusion-limited process.<sup>53</sup> The utilization of the EIS transducer signal in biological sensate practice is predominantly established *via* the involvement of the biological recipient and the selected strain specifically adsorbed from the solution. Equivalence reciprocity proposes a modification in the kinetics of the interfacial electron transfer among conducting electrode sites and the redox probe in solution. The Nyquist plot originating from EIS demonstrates two separate regions: a semicircular section at high frequency, depicting the resistance of the material, and a linear section at low frequency, suggesting the capacitive behavior of the material.<sup>57</sup> A low  $R_{ct}$  value of  $142 \Omega$  was demonstrated for the synthesized composite  $\text{Mn}_3\text{O}_4/\text{rGO}$ , implying effective charge transfer and reduced interfacial resistance. These features emphasize the composite's promising electrochemical properties and its potential as an effective sensing catalyst.



However, the EIS technique was selected for calibration (*i.e.*, concentration-dependent sensing) due to its high sensitivity to interfacial charge transfer resistance ( $R_{ct}$ ), even at very low analyte concentrations. EIS allows for precise monitoring of changes in the electron transfer kinetics upon analyte interaction, offering better resolution for detecting small variations in analyte concentration. This makes EIS particularly effective for constructing calibration curves, especially in label-free or non-faradaic sensing platforms. This electrochemical substitute is then demonstrable *via* supervising the resistance ( $R_{ct}$ ) of charge transfer that is frequently raised in the equivalent fraction, specifying the rise in the number of specific sites to the accessible facet.<sup>58,59</sup> Although the distinction of a biosensor is predominantly anticipated on the precision of the molecular recognition element, varied analytical specifications, for instance, sensitivity, response time, and LoD, firmly rely on the physicochemical characteristics of the transducer, which is conceivably enhanced by utilization. The signal of non-faradaic EIS actuators is primarily attributed to capacitance variations on the electrode-electrolyte edge that are effortlessly detected by the capacitance of the double-layer ( $C_{dl}$ ).<sup>60,61</sup> Consequently, a specific assembled description of individual constituents is significant to attain inflated signal-to-noise ratios, which certify remarkable reliability, optimum sensitivity, quick response time, and low LoD.

A calibration study *via* EIS was accomplished to observe the response of  $\text{Mn}_3\text{O}_4/\text{rGO}/\text{ITO}$  electrodes at varied concentrations of 2,4,6 TCP, presented in Fig. 8(e). Under the optimal detection conditions, a sequence of 2,4,6-TCP with individual concentrations was identified. The calibration measurement determines the linearity in the resistance response at diverse analyte concentrations ranging from 1 to 500  $\mu\text{M}$ . The linearity of the present sensor was verified by procuring the regression equation,  $R^2 = 0.98867$  and  $R^2 = 0.98573$ , as exhibited in Fig. 8(f). The estimated regression value specified the uniformity and linearity of the established sensor. The Nyquist plots shown in Fig. 8(e) correspond to the diameter of the semicircular arc to the electron-transfer impedance. Constituents having modest  $R_{ct}$  values are mostly absolute for active charge transfer. The semicircle of the EIS spectra was fitted to an equivalent circuit to estimate the  $R_{ct}$  value (inset of Fig. 8(f)). The measured  $R_{ct}$  value correlates

with the diameter of the semicircle. The diameter of the semicircle was spotted in the EIS spectrum, indicating a rise in the  $R_{ct}$  at the electrode/electrolyte edge illustrated in Fig. 8(e). The  $R_{ct}$  values were calculated by fitting the semicircle to an equivalent circuit model (inset in Fig. 8(f)). The  $R_{ct}$  value increased from 84  $\Omega$  to 200  $\Omega$  as we increased the concentration of 2,4,6-TCP from 1 to 500  $\mu\text{M}$ . As we increased the concentration, the adsorption of 2,4,6-TCP on the electrode created a barrier blocking active sites and hindering charge transfer. Accumulated 2,4,6-TCP changes the double-layer capacitance and the ionic environment, which slows electron transfer.

The amplitude of the impedance was noted to rise in direct proportion to the 2,4,6-TCP concentration. This phenomenon is attributed to the greater involvement of 2,4,6-TCP molecules in the electrochemical process at the electrode surface, leading to an increase in impedance amplitude. Considering the sensitivity of the electrochemical detection apparatus, elevating the 2,4,6-TCP level expands the detection range of sensors. This enhancement enables the exposure of a broader range of analyte concentrations. The electrochemical sensor displays the linear extent of 2,4,6-TCP detection from 1 to 500  $\mu\text{M}$  with a LoD of 0.038  $\mu\text{M}$  and sensitivity of  $2.17 \Omega \mu\text{M}^{-1} \text{cm}^{-2}$ , consistent with  $R^2 = 0.98867$ , and LoD of 0.048  $\mu\text{M}$  and sensitivity of  $0.56 \Omega \mu\text{M}^{-1} \text{cm}^{-2}$ , consistent with  $R^2 = 0.98573$ . The LOQ values corresponding to  $R^2 = 0.98867$  and  $R^2 = 0.98573$  are 0.13  $\mu\text{M}$  and 0.16  $\mu\text{M}$ , respectively. Subsequently, all these detections were determined and related to other prior studies (Table 1). It affirms that the fabricated sensor demonstrates notable electroanalytical accomplishment compared to other pre-existing 2,4,6-TCP sensors. Its wide linear range exceeds existing sensors by contributing to the extended detection of 2,4,6-TCP concentrations.

The LoD and LOQ are evaluated by employing eqn (18) and (19):

$$\text{LoD} = 3 \times \text{SD}/\text{Slope} \quad (18)$$

$$\text{LOQ} = 10 \times \text{SD}/\text{Slope} \quad (19)$$

where SD is the standard deviation attained from the sensing calibration curve, and the slope signifies the sensitivity of the probe for the analyte.

**Table 1** Comparative table of fabricated 2,4,6-TCP sensor parameters associated with those quantified earlier

Electrode	Technique	Linear range ( $\mu\text{M}$ )	Limit of detection ( $\mu\text{M}$ )	Sensitivity	Reference
CNTs-OH/PtNPs/RhB/GCE	DPV	5.0–175.0	1.55		8
Boron-doped diamond electrode	DPV	1.93–21.3	0.15		7
GC/CeVO <sub>4</sub> electrode	SWV	0.2–60	0.151		62
CuO/Nafion/GCE	DPV	1–120	0.046		63
MIP@SiO <sub>2</sub> @QDs	Fluorescence	5–1000	0.9		64
$\text{Mn}_3\text{O}_4/\text{rGO}/\text{ITO}$	EIS	1–500	0.038	2.17	This work

Note: CNTs – carbon nanotubes, RhB – rhodamine B, GCE – glassy carbon electrode, GC – glassy carbon, ITO – indium tin oxide, MIP – molecularly imprinted polymer, QDs – quantum dots, rGO – reduced graphene oxide.



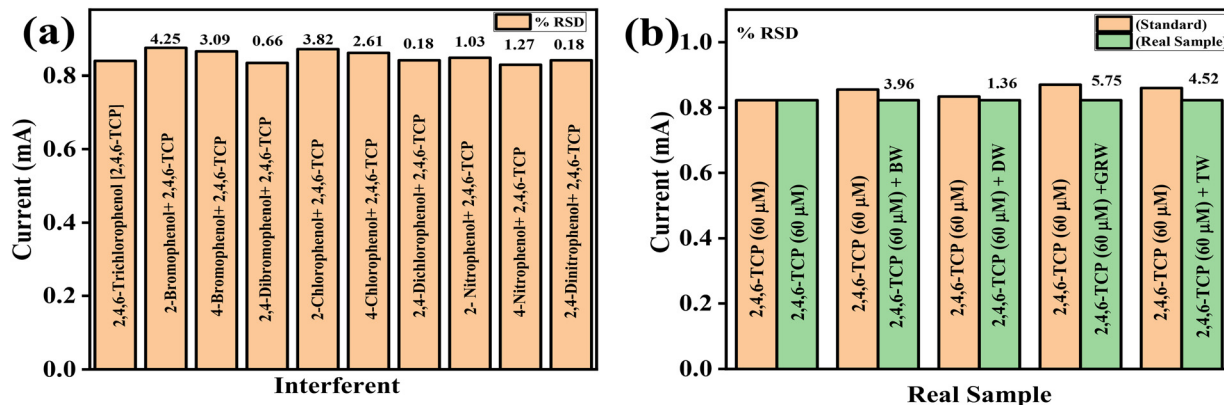


Fig. 9 (a) Bar graph calibration spectrum of the interferent with anodic current (mA). (b) Bar graph calibration plot of the anodic current with different real sample  $\text{Mn}_3\text{O}_4/\text{rGO/ITO}$  electrodes in PBS containing ferri-/ferrocyanide (pH 6) and varying concentrations of 2,4,6-TCP.

### 5.6. Reusability and stability of the $\text{Mn}_3\text{O}_4/\text{rGO/ITO}$ electrode

The reusability of the proposed sensor was measured up to 16 consecutive scans. A reusability study was conducted in a 15 mL PBS solution, which included 20  $\mu\text{L}$  of a 50  $\mu\text{M}$  2,4,6-TCP solution presented in Fig. 8(c). As shown in Fig. 8(c), up to the 14th scan, the % RSD is 5.62, and the % RSD for the 15th and 16th scans is 8.21% and 16.93%, so we can say that the modified electrode is usable up to 16 scans (SI Table S4 and Fig. S5(b)). Moreover, the high reusability of the modified electrode is due to efficient communication between the analyte and the  $\text{Mn}_3\text{O}_4/\text{rGO/ITO}$  electrode. The stability analysis of the electrochemical sensor is significant for the authenticity of sensing devices. The stability of the fabricated  $\text{Mn}_3\text{O}_4/\text{rGO/ITO}$  electrode is up to 60 days, at consistent intervals of 5 days [SI Table S3 and Fig. S5(c)]. During stability analysis, it was found that the % RSD ranged from 0.06% to 0.72%, as displayed fairly in Fig. 8(d), demonstrating that such an electrode is incredibly consistent until the end of the 60 days. After 60 days, the % RSD was 4%, which confirmed that the fabricated electrode was stable during electrochemical analysis.

### 5.7. Interference study of the $\text{Mn}_3\text{O}_4/\text{rGO/ITO}$ electrode

The selectivity of the developed sensing platform was estimated, as this is an essential characteristic for real-world applications. This evaluation implied an assessment of the sensor response in the presence of diverse interfering species that probably coexist with 2,4,6-TCP. The selectivity study is accomplished in the proximity of various interferences like

2-chlorophenol, 4-chlorophenol, 2,4-dichlorophenol, 2-bromophenol, and 4-bromophenol, which were spiked with 2,4,6-TCP. In this regard, CV analysis was carried out by adding 50  $\mu\text{M}$  to each of the interferences. These species were selected due to their common existence in water and the potential to impede the recognition of a target analyte. The corresponding bar graph, presented in Fig. 9(a), exhibits that the existence of an interferent does not affect the activity of 2,4,6-TCP. The observation of peak potential after the addition of 50  $\mu\text{M}$  interferences exhibits no noteworthy changes in peak current or peak potential (SI Table S5 and Fig. S6(a)). This selective response suggests that the  $\text{Mn}_3\text{O}_4/\text{rGO/ITO}$  electrode is selective for the 2,4,6-TCP analyte.

### 5.8. Detection in real samples

The  $\text{Mn}_3\text{O}_4/\text{rGO/ITO}$  electrode was also employed for real environmental samples and was further examined with water samples from different sources *via* CV analysis. Bore well (BW) water, distilled water (DW), Ganga River water (GRW), and tap water (TW) were used as real samples, exhibited in Fig. 9(b). The detection of TCP was accomplished by the standard method of addition. When 2,4,6-TCP was sensed in spiked water samples, the sensor achieved acceptable recovery rates and low relative standard deviations (RSDs). The concentration of 2,4,6-TCP (60  $\mu\text{M}$ ) was spiked into real BW, DW, GRW, and TW *via* utilizing a traditional addition procedure, and recovery rates are presented in Table 2. An assessment of the relevance of the sensor is illustrated through administration by utilizing actual domain

Table 2 2,4,6-TCP concentration detection in real spiked water samples *via* the standard method of addition

Sr. no.	Sample	Added ( $\mu\text{M}$ )	Detected ( $\mu\text{M}$ )	Detection rate (% RSD)
1.	2,4,6-TCP	60	60	0
2.	2,4,6-TCP + BW	60	62.38	3.96
3.	2,4,6-TCP + DW	60	60.82	1.36
4.	2,4,6-TCP + GRW	60	63.45	5.75
5.	2,4,6-TCP + TW	60	62.71	4.52



specimens. Based on these outcomes, we can say that the fabricated  $\text{Mn}_3\text{O}_4$ /rGO/ITO-modified electrode is a feasible device for examining 2,4,6-TCP since its recovery span is within the admissible range (SI Table S6 and Fig. S6(b)). This implies that  $\text{Mn}_3\text{O}_4$ /rGO NCs are effective in the selective detection of 2,4,6-TCP, even in real water samples.

## 6. Conclusion

Here, we demonstrate the successful synthesis of  $\text{Mn}_3\text{O}_4$  NMs as well as  $\text{Mn}_3\text{O}_4$ /rGO NCs as an electrode material for an electrochemical sensing platform.  $\text{Mn}_3\text{O}_4$ /rGO NCs were utilized for the fabrication of a  $\text{Mn}_3\text{O}_4$ /rGO/ITO-modified electrode as an electrochemical sensing scaffold intended for rapid and sensitive detection of 2,4,6-TCP. Here, we accomplished the combined study of photocatalytic and electrocatalytic systems, which led to the detection of 2,4,6-TCP and photocatalytic breakdown of MB with the assistance of  $\text{Mn}_3\text{O}_4$ /rGO NCs in the presence of UV light. The sensor exhibits high selectivity, illustrating nominal interference from coexisting species as well as strong repeatability and stability. These detection techniques emphasize the perspective of the developed sensors for practical environmental applications, providing a reliable method for detecting 2,4,6-TCP.

## Author's contribution

D. S.: data curation, investigation, visualization, writing – original draft. A. K. S.: data curation, validation, writing – original draft. R. V.: data curation, data curation, validation, writing – original draft. J. S.: conceptualization, resources, validation, project administration, supervision, writing review & editing of the original draft.

## Conflicts of interest

All authors declare no conflicts of interest.

## Data availability

The data supporting this article have been included as part of the SI. Supplementary Information: The SI included characterization technique information, Results, and discussion of GO and rGO, XRD, Raman, FTIR, TEM, SEM, and EDAX of GO and rGO. Experimental details of photocatalytic degradation experiments. Scan rate analysis table, complete calculation with % recovery and % RSD of response time, stability, reusability analysis of  $\text{Mn}_3\text{O}_4$ /rGO/ITO electrode. Interference, real sample analysis, complete calculation with % recovery and % RSD of the 2,4,6-TCP on the  $\text{Mn}_3\text{O}_4$ /rGO/ITO electrode. TEM, HR-TEM, SEM, EDAX of  $\text{Mn}_3\text{O}_4$ ,  $\text{Mn}_3\text{O}_4$ /rGO, and TEM, SEM, EDAX of GO and rGO. See DOI: <https://doi.org/10.1039/D5LF00149H>

## Acknowledgements

This work received no specific grant from public, commercial, or not-for-profit funding agencies. D. S. acknowledges CSIR, New Delhi, for financial support under the program CSIR-09/0013(17524)/2024-EMR-I. A. K. S. is thankful to BHU for funding during this work. R. V. acknowledges the financial support provided by DBT for the awarding DBT-BioCare women scientist (Award no. 102/IFD/SAN/2081/2023-2024). J. S. acknowledges BHU for offering a seed grant along with a Bridge grant under the MoE, Govt. of India, Institute of Eminence (IoE), under Dev. Scheme No. 60317 & 6031A.

## References

- 1 X. Yuan, N. Gao, X. Gao, D. Qiu, R. Xu and Z. Sun, *et al.*, Nanopyramid boron-doped diamond electrode realizing nanomolar detection limit of 4-nonylphenol, *Sens. Actuators, B*, 2019, **281**, 830–836, DOI: [10.1016/j.snb.2018.11.011](https://doi.org/10.1016/j.snb.2018.11.011).
- 2 J.-L. Zhao, Z. Huang, Q.-Q. Zhang, L. Ying-He, T.-T. Wang and Y.-Y. Yang, *et al.*, Distribution and mass loads of xenoestrogens bisphenol a, 4-nonylphenol, and 4-tert-octylphenol in rainfall runoff from highly urbanized regions: A comparison with point sources of wastewater, *J. Hazard. Mater.*, 2021, **401**, 123747, DOI: [10.1016/j.jhazmat.2020.123747](https://doi.org/10.1016/j.jhazmat.2020.123747).
- 3 L. V. Trandafilović, D. J. Jovanović, X. Zhang, S. Ptasińska and M. D. Dramićanin, Enhanced photocatalytic degradation of methylene blue and methyl orange by  $\text{ZnO}:\text{Eu}$  nanoparticles, *Appl. Catal., B*, 2017, **203**, 740–752, DOI: [10.1016/j.apcatb.2016.10.063](https://doi.org/10.1016/j.apcatb.2016.10.063).
- 4 B. H. Hameed, I. A. W. Tan and A. L. Ahmad, Adsorption isotherm, kinetic modeling and mechanism of 2,4,6-trichlorophenol on coconut husk-based activated carbon, *Chem. Eng. J.*, 2008, **144**(2), 235–244, DOI: [10.1016/j.cej.2008.01.028](https://doi.org/10.1016/j.cej.2008.01.028).
- 5 A. R. Fontana, Analytical methods for determination of cork-taint compounds in wine, *TrAC, Trends Anal. Chem.*, 2012, **37**, 135–147, DOI: [10.1016/j.trac.2012.03.012](https://doi.org/10.1016/j.trac.2012.03.012).
- 6 K.-Y. Hwa, A. Ganguly, A. Santhan and T. S. Kanna Sharma, Vanadium selenide decorated reduced graphene oxide nanocomposite: A co-active catalyst for the detection of 2,4,6-Trichlorophenol, *Chemosphere*, 2021, **282**, 130874, DOI: [10.1016/j.chemosphere.2021.130874](https://doi.org/10.1016/j.chemosphere.2021.130874).
- 7 E. D. P. Schwab, S. V. de Almeida, M. L. Felsner, E. G. de Castro and A. Galli, Determination of 2,4,6-TRICHLOROPHENOL in Beverages Using Voltammetry: Optimization and Validation Studies, *Food Anal. Methods*, 2020, **13**(4), 1000–1007, DOI: [10.1007/s12161-020-01716-4](https://doi.org/10.1007/s12161-020-01716-4).
- 8 X. Zhu, K. Zhang, D. Wang, D. Zhang, X. Yuan and J. Qu, Electrochemical sensor based on hydroxylated carbon nanotubes/platinum nanoparticles/rhodamine B composite for simultaneous determination of 2,4,6-trichlorophenol and 4-chlorophenol, *J. Electroanal. Chem.*, 2018, **810**, 199–206, DOI: [10.1016/j.jelechem.2018.01.017](https://doi.org/10.1016/j.jelechem.2018.01.017).
- 9 B. H. Hameed, I. A. W. Tan and A. L. Ahmad, Preparation of oil palm empty fruit bunch-based activated carbon for removal



of 2,4,6-trichlorophenol: Optimization using response surface methodology, *J. Hazard. Mater.*, 2009, **164**(2–3), 1316–1324, DOI: [10.1016/j.jhazmat.2008.09.042](https://doi.org/10.1016/j.jhazmat.2008.09.042).

10 D. Krishnaiah, S. M. Anisuzzaman, A. Bono and R. Sarbatly, Adsorption of 2,4,6-trichlorophenol (TCP) onto activated carbon, *J. King Saud Univ., Sci.*, 2013, **25**(3), 251–255, DOI: [10.1016/j.jksus.2012.10.001](https://doi.org/10.1016/j.jksus.2012.10.001).

11 M. Moztahida and D. S. Lee, Photocatalytic degradation of methylene blue with P25/graphene/polyacrylamide hydrogels: Optimization using response surface methodology, *J. Hazard. Mater.*, 2020, **400**, 123314, DOI: [10.1016/j.jhazmat.2020.123314](https://doi.org/10.1016/j.jhazmat.2020.123314).

12 M. Bora Akin and M. Oner, Photodegradation of methylene blue with sphere-like ZnO particles prepared via aqueous solution, *Ceram. Int.*, 2013, **39**(8), 9759–9762, DOI: [10.1016/j.ceramint.2013.05.024](https://doi.org/10.1016/j.ceramint.2013.05.024).

13 Y. Paz, Preferential photodegradation – why and how?, *C. R. Chim.*, 2005, **9**(5–6), 774–787, DOI: [10.1016/j.crci.2005.03.032](https://doi.org/10.1016/j.crci.2005.03.032).

14 J. T. Adeleke, T. Theivasanthi, M. Thiruppathi, M. Swaminathan, T. Akomolafe and A. B. Alabi, Photocatalytic degradation of methylene blue by ZnO/NiFe2O4 nanoparticles, *Appl. Surf. Sci.*, 2018, **455**, 195–200, DOI: [10.1016/j.apsusc.2018.05.184](https://doi.org/10.1016/j.apsusc.2018.05.184).

15 A. Hamrouni, H. Lachheb and A. Houas, Synthesis, characterization and photocatalytic activity of ZnO-SnO<sub>2</sub> nanocomposites, *Mater. Sci. Eng., B*, 2013, **178**(20), 1371–1379, DOI: [10.1016/j.mseb.2013.08.008](https://doi.org/10.1016/j.mseb.2013.08.008).

16 R. M. Black and B. Muir, Derivatisation reactions in the chromatographic analysis of chemical warfare agents and their degradation products, *J. Chromatogr. A*, 2003, **1000**(1–2), 253–281, DOI: [10.1016/S0021-9673\(03\)00183-3](https://doi.org/10.1016/S0021-9673(03)00183-3).

17 J.-T. Huang, L. Alquier, J. P. Kaisa, G. Reed, T. Gilmor and G. Vas, Method development and validation for the determination of 2,4,6-tribromoanisole, 2,4,6-tribromophenol, 2,4,6-trichloroanisole, and 2,4,6-trichlorophenol in various drug products using stir bar sorptive extraction and gas chromatography–tandem mass spectr., *J. Chromatogr. A*, 2012, **1262**, 196–204, DOI: [10.1016/j.chroma.2012.09.010](https://doi.org/10.1016/j.chroma.2012.09.010).

18 K. C. Christoforidis, M. Louloudi and Y. Deligiannakis, Complete dechlorination of pentachlorophenol by a heterogeneous SiO<sub>2</sub>–Fe-porphyrin catalyst, *Appl. Catal., B*, 2010, **95**(3–4), 297–302, DOI: [10.1016/j.apcatb.2010.01.007](https://doi.org/10.1016/j.apcatb.2010.01.007).

19 M. Pera-Titus, V. García-Molina, M. A. Baños, J. Giménez and S. Esplugas, Degradation of chlorophenols by means of advanced oxidation processes: a general review, *Appl. Catal., B*, 2004, **47**(4), 219–256, DOI: [10.1016/j.apcatb.2003.09.010](https://doi.org/10.1016/j.apcatb.2003.09.010).

20 A. Remes, A. Pop, F. Manea, A. Baciu, S. J. Picken and J. Schoonman, Electrochemical Determination of pentachlorophenol in Water on a Multi-Wall Carbon Nanotubes-Epoxy Composite Electrode, *Sensors*, 2012, **12**(6), 7033–7046, DOI: [10.3390/s120607033](https://doi.org/10.3390/s120607033).

21 J. Liang, S. Yang, S. Luo, C. Liu and Y. Tang, Ultrasensitive electrochemiluminescent detection of pentachlorophenol using a multiple amplification strategy based on a hybrid material made from quantum dots, graphene, and carbon nanotubes, *Microchim. Acta*, 2014, **181**(7–8), 759–765, DOI: [10.1007/s00604-013-1081-9](https://doi.org/10.1007/s00604-013-1081-9).

22 J.-F. Peng, J.-F. Liu, X.-L. Hu and G.-B. Jiang, Direct determination of chlorophenols in environmental water samples by hollow fiber supported ionic liquid membrane extraction coupled with high-performance liquid chromatography, *J. Chromatogr. A*, 2007, **1139**(2), 165–170, DOI: [10.1016/j.chroma.2006.11.006](https://doi.org/10.1016/j.chroma.2006.11.006).

23 J. I. Cacho, N. Campillo, P. Viñas and M. Hernández-Córdoba, Stir bar sorptive extraction polar coatings for the determination of chlorophenols and chloroanisoles in wines using gas chromatography and mass spectrometry, *Talanta*, 2014, **118**, 30–36, DOI: [10.1016/j.talanta.2013.09.047](https://doi.org/10.1016/j.talanta.2013.09.047).

24 E. Morita and E. Nakamura, Solid-Phase Extraction of Antipyrine Dye for Spectrophotometric Determination of Phenolic Compounds in Water, *Anal. Sci.*, 2011, **27**(5), 489–492, DOI: [10.2116/analsci.27.489](https://doi.org/10.2116/analsci.27.489).

25 W. Szczepaniak, B. Czyżowicz and M. Ren, Voltammetric determination of Prometrine in soil and water, *Anal. Chim. Acta*, 1995, **305**(1–3), 207–211, DOI: [10.1016/0003-2670\(94\)00454-T](https://doi.org/10.1016/0003-2670(94)00454-T).

26 Y. Song, J. Chen, M. Sun, C. Gong, Y. Shen and Y. Song, *et al.*, A simple electrochemical biosensor based on AuNPs/MPS/Au electrode sensing layer for monitoring carbamate pesticides in real samples, *J. Hazard. Mater.*, 2016, **304**, 103–109, DOI: [10.1016/j.jhazmat.2015.10.058](https://doi.org/10.1016/j.jhazmat.2015.10.058).

27 M. Maria Stanley, V. A. Sherlin, S.-F. Wang, J. N. Baby, B. Sriram and M. George, Deep eutectic solvent assisted synthesis of molybdenum nitride entrapped graphene aerogel heterostructure with enhanced electrochemical behavior for ronidazole drug detection, *J. Mol. Liq.*, 2023, **375**, 121308, DOI: [10.1016/j.molliq.2023.121308](https://doi.org/10.1016/j.molliq.2023.121308).

28 B. Sriram, S. Kogularasu, S.-F. Wang and J.-K. Sheu, Deep Eutectic Solvent-Mediated Synthesis of Spinel Zinc Chromite Nanoparticles: A Simple Label-Free Electrochemical Sensor for Dopamine and Ascorbic Acid, *ACS Appl. Nano Mater.*, 2023, **6**(19), 17593–17602, DOI: [10.1021/acsanm.3c02775](https://doi.org/10.1021/acsanm.3c02775).

29 N. Sohal, B. Maity, N. P. Shetti and S. Basu, Biosensors Based on MnO<sub>2</sub> Nanostructures: A Review, *ACS Appl. Nano Mater.*, 2021, **4**(3), 2285–2302, DOI: [10.1021/acsanm.0c03380](https://doi.org/10.1021/acsanm.0c03380).

30 S. V. Selvi, A. Krishnapandi, R. Damastuti, A. Prasannan, S.-T. Liang and P.-D. Hong, *et al.*, Effectively Reinforced  $\alpha$ -Bi<sub>2</sub>O<sub>3</sub> MPs/PDA-RGO Sensor for Selective Modality Sensing of a Hazardous Phenolic Compound, *J. Agric. Food Chem.*, 2023, **71**(51), 20563–20574, DOI: [10.1021/acs.jafc.3c03488](https://doi.org/10.1021/acs.jafc.3c03488).

31 V. H. Nguyen, C. Lamiel, D. Kharismadewi, V. C. Tran and J.-J. Shim, Covalently bonded reduced graphene oxide/polyaniline composite for electrochemical sensors and capacitors, *J. Electroanal. Chem.*, 2015, **758**, 148–155, DOI: [10.1016/j.jelechem.2015.10.023](https://doi.org/10.1016/j.jelechem.2015.10.023).

32 H. Chai, J. Xu, Ji Han, Y. Su, Z. Sun and D. Jia, *et al.*, Facile synthesis of Mn<sub>3</sub>O<sub>4</sub>-rGO hybrid materials for the high-performance electrocatalytic reduction of oxygen, *J. Colloid Interface Sci.*, 2017, **488**, 251–257, DOI: [10.1016/j.jcis.2016.10.049](https://doi.org/10.1016/j.jcis.2016.10.049).



33 Y. Hou, Z. Wen, S. Cui, S. Ci, S. Mao and J. Chen, An Advanced Nitrogen-Doped Graphene/Cobalt-Embedded Porous Carbon Polyhedron Hybrid for Efficient Catalysis of Oxygen Reduction and Water Splitting, *Adv. Funct. Mater.*, 2015, 25(6), 872–882, DOI: [10.1002/adfm.201403657](https://doi.org/10.1002/adfm.201403657).

34 J. Yan, Z. Fan, T. Wei, W. Qian, M. Zhang and F. Wei, Fast and reversible surface redox reaction of graphene–MnO<sub>2</sub> composites as supercapacitor electrodes, *Carbon*, 2010, 48(13), 3825–3833, DOI: [10.1016/j.carbon.2010.06.047](https://doi.org/10.1016/j.carbon.2010.06.047).

35 L.-X. Yang, Y. Liang, H. Chen, Y.-F. Meng and W. Jiang, Controlled synthesis of Mn<sub>3</sub>O<sub>4</sub> and MnCO<sub>3</sub> in a solvothermal system, *Mater. Res. Bull.*, 2009, 44(8), 1753–1759, DOI: [10.1016/j.materresbull.2009.03.004](https://doi.org/10.1016/j.materresbull.2009.03.004).

36 M. Bernard, A. Hugot-Le Goff, B. V. Thi and S. Cordoba de Torresi, Electrochromic Reactions in Manganese Oxides: I. Raman Analysis, *J. Electrochem. Soc.*, 1993, 140(11), 3065–3070, DOI: [10.1149/1.2220986](https://doi.org/10.1149/1.2220986).

37 C. Julien, M. Massot and C. Poinsignon, Lattice vibrations of manganese oxides, *Spectrochim. Acta, Part A*, 2004, 60(3), 689–700, DOI: [10.1016/S1386-1425\(03\)00279-8](https://doi.org/10.1016/S1386-1425(03)00279-8).

38 A. C. Ferrari and J. Robertson, Raman spectroscopy of amorphous, nanostructured, diamond-like carbon, and nanodiamond, *Philos. Trans. R. Soc., A*, 2004, 362(1824), 2477–2512, DOI: [10.1098/rsta.2004.1452](https://doi.org/10.1098/rsta.2004.1452).

39 Z. Li, Y. Mi, X. Liu, S. Liu, S. Yang and J. Wang, Flexible graphene/MnO<sub>2</sub> composite papers for supercapacitor electrodes, *J. Mater. Chem.*, 2011, 21(38), 14706, DOI: [10.1039/c1jm11941a](https://doi.org/10.1039/c1jm11941a).

40 Y. Chen, Y. Zhang, D. Geng, R. Li, H. Hong and J. Chen, *et al.*, One-pot synthesis of MnO<sub>2</sub>/graphene/carbon nanotube hybrid by chemical method, *Carbon*, 2011, 49(13), 4434–4442, DOI: [10.1016/j.carbon.2011.06.046](https://doi.org/10.1016/j.carbon.2011.06.046).

41 B. K. Vijayan, N. M. Dimitrijevic, D. Finkelstein-Shapiro, J. Wu and K. A. Gray, Coupling Titania Nanotubes and Carbon Nanotubes To Create Photocatalytic Nanocomposites, *ACS Catal.*, 2012, 2(2), 223–229, DOI: [10.1021/cs200541a](https://doi.org/10.1021/cs200541a).

42 A. K. Singh, P. K. Vishwakarma, S. K. Pandey, R. Pratap, R. Giri and A. Srivastava, A comparative study of band gap engineered in-situ and ex-situ MWCNTs/TiO<sub>2</sub> heterostructures for their enhanced photocatalytic activity under visible light, *Inorg. Chem. Commun.*, 2023, 150, 110540, DOI: [10.1016/j.inoche.2023.110540](https://doi.org/10.1016/j.inoche.2023.110540).

43 S. Ghosh, S. Basu and M. Baskey, Decorating mechanism of Mn<sub>3</sub>O<sub>4</sub> nanoparticles on reduced graphene oxide surface through reflux condensation method to improve photocatalytic performance, *J. Mater. Sci.: Mater. Electron.*, 2017, 28(23), 17860–17870, DOI: [10.1007/s10854-017-7727-3](https://doi.org/10.1007/s10854-017-7727-3).

44 G. S. Gund, D. P. Dubal, B. H. Patil, S. S. Shinde and C. D. Lokhande, Enhanced activity of chemically synthesized hybrid graphene oxide/Mn<sub>3</sub>O<sub>4</sub> composite for high performance supercapacitors, *Electrochim. Acta*, 2013, 92, 205–215, DOI: [10.1016/j.electacta.2012.12.120](https://doi.org/10.1016/j.electacta.2012.12.120).

45 A. Giri, N. Goswami, C. Sasmal, N. Polley, D. Majumdar and S. Sarkar, *et al.*, Unprecedented catalytic activity of Mn<sub>3</sub>O<sub>4</sub> nanoparticles: potential lead of a sustainable therapeutic agent for hyperbilirubinemia, *RSC Adv.*, 2014, 4(10), 5075, DOI: [10.1039/c3ra45545a](https://doi.org/10.1039/c3ra45545a).

46 D. Wang, Y. Li, Q. Wang and T. Wang, Facile Synthesis of Porous Mn<sub>3</sub>O<sub>4</sub> Nanocrystal–Graphene Nanocomposites for Electrochemical Supercapacitors, *Eur. J. Inorg. Chem.*, 2012, 2012(4), 628–635, DOI: [10.1002/ejic.201100983](https://doi.org/10.1002/ejic.201100983).

47 J. Duan, S. Chen, S. Dai and S. Z. Qiao, Shape Control of Mn<sub>3</sub>O<sub>4</sub> Nanoparticles on Nitrogen-Doped Graphene for Enhanced Oxygen Reduction Activity, *Adv. Funct. Mater.*, 2014, 24(14), 2072–2078, DOI: [10.1002/adfm.201302940](https://doi.org/10.1002/adfm.201302940).

48 F. Gao, J. Qu, Z. Zhao, Q. Zhou, B. Li and J. Qiu, A green strategy for the synthesis of graphene supported Mn<sub>3</sub>O<sub>4</sub> nanocomposites from graphitized coal and their supercapacitor application, *Carbon*, 2014, 80, 640–650, DOI: [10.1016/j.carbon.2014.09.008](https://doi.org/10.1016/j.carbon.2014.09.008).

49 Z.-Y. Tian, P. Mountapmbeme Kouotou, N. Bahlawane and P. H. Tchoua Ngamou, Synthesis of the Catalytically Active Mn<sub>3</sub>O<sub>4</sub> Spinel and Its Thermal Properties, *J. Phys. Chem. C*, 2013, 117(12), 6218–6224, DOI: [10.1021/jp312444s](https://doi.org/10.1021/jp312444s).

50 W. Zhang, X. Guo, J. Zhao, Y. Zheng, H. Xie and Z. Zhang, *et al.*, High performance Flower-Like Mn<sub>3</sub>O<sub>4</sub>/rGO composite for supercapacitor applications, *J. Electroanal. Chem.*, 2022, 910, 116170, DOI: [10.1016/j.jelechem.2022.116170](https://doi.org/10.1016/j.jelechem.2022.116170).

51 S. Soylemez, S. O. Hacioglu, M. Kesik, H. Unay, A. Cirpan and L. Toppare, A Novel and Effective Surface Design: Conducting Polymer/β-Cyclodextrin Host–Guest System for Cholesterol Biosensor, *ACS Appl. Mater. Interfaces*, 2014, 6(20), 18290–18300, DOI: [10.1021/am5054493](https://doi.org/10.1021/am5054493).

52 D. Singh, R. Verma, K. R. Singh, M. Srivastava, R. P. Singh and J. Singh, Biogenic synthesis of CuO/ZnO nanocomposite from Bauhinia variegata flower extract for highly sensitive electrochemical detection of vitamin B2, *Biomater. Adv.*, 2024, 161, 213898, DOI: [10.1016/j.bioadv.2024.213898](https://doi.org/10.1016/j.bioadv.2024.213898).

53 A. C. Lazanas and M. I. Prodromidis, Electrochemical Impedance Spectroscopy-A Tutorial, *ACS Meas. Sci. Au*, 2023, 3(3), 162–193, DOI: [10.1021/acsmmeasuresci.2c00070](https://doi.org/10.1021/acsmmeasuresci.2c00070).

54 J. Wang, *Analytical Electrochemistry*, Wiley, 2006, DOI: [10.1002/0471790303](https://doi.org/10.1002/0471790303).

55 E. Laviron, General expression of the linear potential sweep voltammogram in the case of diffusionless electrochemical systems, *J. Electroanal. Chem. Interfacial Electrochem.*, 1979, 101(1), 19–28, DOI: [10.1016/S0022-0728\(79\)80075-3](https://doi.org/10.1016/S0022-0728(79)80075-3).

56 A. P. Brown and F. C. Anson, Cyclic and differential pulse voltammetric behavior of reactants confined to the electrode surface, *Anal. Chem.*, 1977, 49(11), 1589–1595, DOI: [10.1021/ac50019a033](https://doi.org/10.1021/ac50019a033).

57 H. N. Jayasimha, K. G. Chandrappa, P. F. Sanaulla and V. G. Dileepkumar, Green synthesis of CuO nanoparticles: A promising material for photocatalysis and electrochemical sensor, *Sens. Int.*, 2024, 5, 100254, DOI: [10.1016/j.sint.2023.100254](https://doi.org/10.1016/j.sint.2023.100254).

58 R. Elshafey, C. Tlili, A. Abulrob, A. C. Tavares and M. Zourob, Label-free impedimetric immunosensor for ultrasensitive detection of cancer marker Murine double



minute 2 in brain tissue, *Biosens. Bioelectron.*, 2013, **39**(1), 220–225, DOI: [10.1016/j.bios.2012.07.049](https://doi.org/10.1016/j.bios.2012.07.049).

59 R. Ohno, H. Ohnuki, H. Wang, T. Yokoyama, H. Endo and D. Tsuya, *et al.*, Electrochemical impedance spectroscopy biosensor with interdigitated electrode for detection of human immunoglobulin A, *Biosens. Bioelectron.*, 2013, **40**(1), 422–426, DOI: [10.1016/j.bios.2012.07.052](https://doi.org/10.1016/j.bios.2012.07.052).

60 M. S. Góes, H. Rahman, J. Ryall, J. J. Davis and P. R. Bueno, A Dielectric Model of Self-Assembled Monolayer Interfaces by Capacitive Spectroscopy, *Langmuir*, 2012, **28**(25), 9689–9699, DOI: [10.1021/la301281y](https://doi.org/10.1021/la301281y).

61 V. Tsouti, C. Boutopoulos, I. Zergioti and S. Chatzandroulis, Capacitive microsystems for biological sensing, *Biosens. Bioelectron.*, 2011, **27**(1), 1–11, DOI: [10.1016/j.bios.2011.05.047](https://doi.org/10.1016/j.bios.2011.05.047).

62 R. Morozov, V. Avdin, G. Lychkin, D. Uchaev, I. Vakhitov and D. Stanković, Facile prepared high purity Cerium vanadate for simultaneous electrochemical detection of p-nitrophenol and 2,4,6-trichlorophenol, *J. Phys. Chem. Solids*, 2025, **196**, 112355, DOI: [10.1016/j.jpcs.2024.112355](https://doi.org/10.1016/j.jpcs.2024.112355).

63 J. A. Buledi, A. R. Solangi, S. Q. Memon, S. I. Haider, S. Ameen and N. H. Khand, *et al.*, Nonenzymatic Electrochemical Detection of 2,4,6-Trichlorophenol Using CuO/Nafion/GCE: A Practical Sensor for Environmental Toxicants, *Langmuir*, 2021, **37**(10), 3214–3222, DOI: [10.1021/acs.langmuir.1c00165](https://doi.org/10.1021/acs.langmuir.1c00165).

64 Y. Liu, P. Chen, S. Zheng, Y. Xing and C. Huang, Novel fluorescent sensor using molecularly imprinted silica microsphere-coated CdSe@CdS quantum dots and its application in the detection of 2,4,6-trichlorophenol from environmental water samples, *Luminescence*, 2019, **34**(7), 680–688, DOI: [10.1002/bio.3653](https://doi.org/10.1002/bio.3653).

